Historic, Archive Document

Do not assume content reflects current
scientific knowledge, policies, or practices.

United States
Department of
Agriculture

Forest Service

**Rocky Mountain
Forest and Range
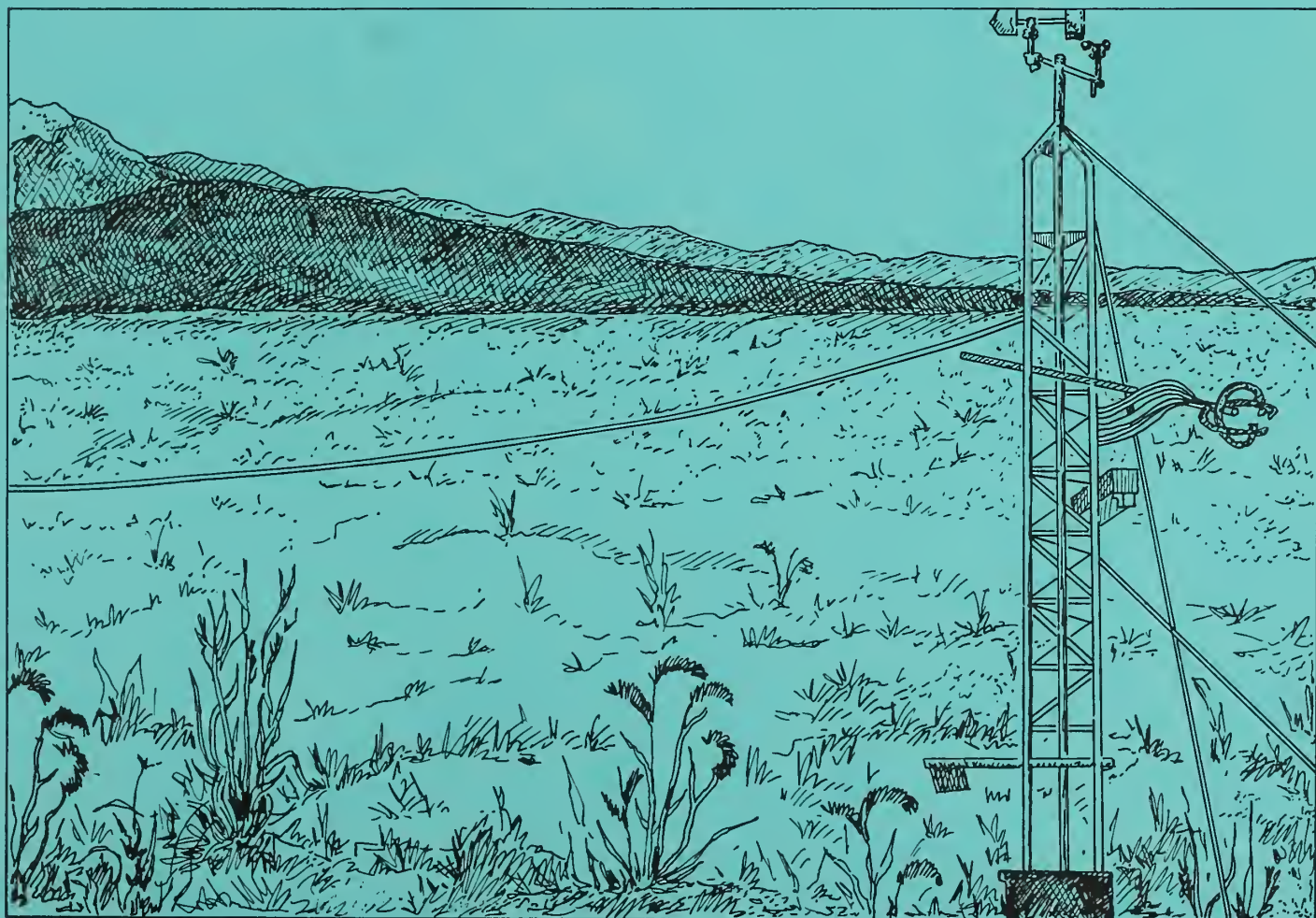Experiment Station**

Fort Collins,
Colorado 80526

**Research Paper
RM-282**

Initial Results from the Pawnee Eddy Correlation System for Dry Acid Deposition Research

**Karl Zeller
William Massman
David Stocker
Douglas G. Fox
Donald Stedman
Donald Hazlett**

Abstract

The Pawnee Grassland Eddy Correlation Dry Deposition Project is described. Instrumentation, methods of analysis, and initial data and research findings are presented. Data from this eddy correlation system show agreement with (a) previous observations of deposition velocities for atmospheric ozone, NO_2, and NO_x; (b) micrometeorological theory; and (c) micrometeorological site characteristics.

Initial Results from the Pawnee Eddy Correlation System for Dry Acid Deposition Research

Karl Zeller, Meteorologist
Rocky Mountain Forest and Range Experiment Station[1]
William Massman, Meteorologist
Rocky Mountain Forest and Range Experiment Station[1]
David Stocker, Research Associate
Denver University[2]
Douglas G. Fox, Chief Meteorologist
Rocky Mountain Forest and Range Experiment Station[1]
Donald Stedman, Professor
Denver University[2]
Donald Hazlett, Research Associate
Natural Resource Ecology Laboratory[3]

[1]Headquarters is in Fort Collins, in cooperation with Colorado State University.
[2]Chemistry Department, Denver, Colorado.
[3]Colorado State University, Fort Collins, Colorado.

Contents

Initial Results from the
Pawnee Eddy Correlation System
for Dry Acid Deposition Research

Karl Zeller, William Massman, David Stocker, Douglas G. Fox,
Donald Stedman, and Donald Hazlett

MANAGEMENT IMPLICATIONS

The deposition of sulphur (S) and nitrogen (N) compounds is the focus of a large research program being carried on currently throughout the United States. The objective of this research program is to determine what loadings of S and N (in kilograms/hectare/year) will cause adverse ecological effects and to quantify these effects. Furthermore, research on forested ecosystems suggest that ozone, a pollutant photochemically generated from emissions of nitrogen oxides and hydrocarbons, must also be included with S and N in determining forest health.

Depending upon climate and the ambient atmospheric environment, S, N, and ozone may be deposited by either dry "processes" or by precipitation. This paper discusses only the dry deposition process.

At first glance measuring dry deposition might seem to be an easy task; for example, simply put out a bucket and measure what falls in when it is not raining. However, dry deposition measurements are not simple because the surfaces on which dry deposition occurs may themselves actively be removing the pollutant. Therefore, simple passive monitoring is not adequate for a full description of the dry deposition process. Some understanding of the nature of the underlying surface is also required.

The most accurate techniques for measuring dry deposition employ aerodynamic methods. Essentially these involve measuring how much pollution passes by a fixed level in the atmosphere. This procedure works best when the vegetation is uniform and the terrain is flat. The research reported on in this paper represents a test of the aerodynamic method known as eddy correlation under circumstances where it is expected to work well.

Eventually, we plan to use eddy correlation to make dry deposition measurements in typical alpine and subalpine ecosystems. These eddy correlation measurements will then be used to confirm simpler technologies for routine measurements of the levels of S, N, and ozone present and depositing to forested lands.

INTRODUCTION

Awareness that acid precipitation and dry deposition of acid gases and aerosols can have potentially significant impacts on the biota at the earth's surface has grown steadily in recent years (NAPAP 1987, Wetstone 1980). However, the processes by which pollutants are transported to and subsequently interact with the biota and the soils, and the influence that these pollutants can have upon the biota, remain largely unknown. In an effort to better understand these processes the USDA Forest Service, Rocky Mountain Forest and Range Experiment Station (USFS/RMFRES), Atmospheric Deposition Research Project, has undertaken a dry deposition monitoring program. This paper describes that program, outlines the data analysis methods used, and presents some initial results from our measurements.

This report specifically details efforts to implement the eddy correlation method of estimating the dry deposition fluxes of ozone, NO_2, and NO_x. This micrometeorologically based method uses a direct measurement of the covariance between the fluctuating vertical velocity and the fluctuating concentration of the acid gas to determine the vertical flux (or rate of deposition per unit of surface area) of the pollutant to the underlying surface. The eddy correlation technique is not the only method available for estimating fluxes [Wesely and Hicks (1977) and Businger (1986) give reviews of this and other meteorological methods]; but, it does have several advantages over the other approaches. It is the most fundamental of the different meteorological methods because it requires the fewest assumptions and, at present, is also the only method capable of providing a direct measure of the vertical flux of a quantity to or from the underlying surface. It is important to note that the eddy correlation flux data, although taken at a fixed point, can be considered to be the integration of the surface fluxes from some distance upstream. A disadvantage of the eddy correlation method is that it is the most demanding technically because dry deposition rates are particularly difficult to measure. For example, Sehmel (1984) lists 51 separate variables that can affect dry deposition rates.

The paper first gives the physical and biological description of our research site and an overview of the instrumentation used before addressing the errors associated with measurement systems in general and this system in particular. Then, initial results of the data analysis are presented. Also included are several appendixes that detail important aspects of our overall effort.

PAWNEE RESEARCH SITE DESCRIPTION

The Pawnee Project eddy correlation research site is 50 km northeast of Fort Collins, CO, at the Central Plains Experimental Range (CPER), a research area adjacent to and west of the Pawnee National Grasslands. The CPER is a 6,500-ha area of shortgrass prairie that is ad-

ministered by the Agricultural Research Service of the USDA. Also located at the CPER is a long-term ecological research (LTER) shortgrass steppe research station (Halfpenny and Ingraham 1984). The LTER station is managed by Colorado State University (CSU) and is funded by the National Science Foundation. The exact CPER location of the eddy correlation research site is within a 6-ha grazing exclosure in Weld County (section 27, 1,641 m elevation, latitude 40°28′23″N, and longitude 104°45′15″W.) (Fig. 1). This exclosure was established in 1969 as an appropriate and "representative" site for meteorological instrumentation. The area is level, bordered on all sides by gently undulating plains, and is not near major ridges or bluffs that would seriously influence measurements.

Vegetation on the CPER is dominated by shortgrasses (64%), succulents (20%), and half-shrubs (8%). The immediate area surrounding the eddy correlation instrumentation is dominated by blue grama grass (*Bouteloua gracilis*), the major plant community type of the shortgrass steppe area in eastern Colorado (Lauenroth and Milchunas 1985). Blue grama, a warm season grass that exhibits the dicarboxylic acid biochemical pathway of CO_2 fixation, has an optimum photosynthetic temperature (when soil water is not limiting) of between 26°C and 33°C (Brown and Trlica 1974). Also present, but less common, are *Bouteloua gracilis-Agropyron smithii* (blue grama-western wheatgrass) plant communities. Western wheatgrass is a "cool season grass" (greatest growth during the spring and early summer) that is infrequent in the research vicinity. However, *Stipa comata* (needleand-thread), also a cool season grass, is common and nearly a codominant in the immediate vicinity of the Pawnee Project instrumentation tower. The most frequent forbs in the area are *Opuntia polyacantha* (pricklypear cactus), *Gutierrezia sarothrae* (snakeweed), and *Artemisia frigida* (fringed sage). Table 1 provides further details on species composition within the exclosure site.

The maximum total green leaf area index (LAI) attained from studies of various vegetation types at the

Table 1.—Plant species in the immediate area of the NOAA/eddy correlation experimentation.[a]

Family	Species[b]
Cactacae	*Opuntia polyacantha* Haw.[*]
Chenopodiaceae	*Chenopodium album* L.
Chenopodiaceae	*Kochia scoparia* (L.) Schrad.
Commeliniaceae	*Tradescantia occidentalis* (Britt.) Smyth
Compositae	*Artemisia frigida* Willd.[*]
Compositae	*Chrysothamnus nauseosus* (Pall.) Britt.
Compositae	*Cirsium undulatum* (Nutt.) Spreng.
Compositae	*Grindelia squarrosa* (Pursh) Dunal
Compositae	*Gutierrezia sarotharae* (Pursh)[*] Britt. + Rusby
Compositae	*Senecio tridenticulatus* Rydb.
Compositae	*Thelesperma filifolium* (Hook.) A. Gray
Compositae	*Tragopogon dubius* Scop.
Convolvulaceae	*Evolvulus nuttallianus* R. + S.
Cruciferae	*Lepidium densiflorum* Schrad.
Cyperaceae	*Carex eleocharis* Bailey
Cyperaceae	*Carex filifolia* Nutt.
Graminae	*Aristida longiseta* Steud.[*]
Graminae	*Bouteloua gracilis* (H.B.K.) Steud.[**]
Graminae	*Buchloe dactyloides* (Nutt.) Engelm.[*]
Graminae	*Sporobolus cryptandrus* (Torr.) Gray[*]
Graminae	*Stipa comata* Trin. + Rupr.[*]
Malvaveae	*Sphaeralcea coccinea* (Pursh) Rydb.[*]
Polygonaceae	*Eriogonum effusum* Nutt.

[a]*Nomenclature taken from Flora of the Great Plains, 1986, T.M. Barkley et al. (editors), Great Plains Flora Association, University Press of Kansas, Lawrence, Kansas, 1392 p.*
[b]*Frequency of occurrence indicated as follows:*
[*]*Common in tower vicinity.*
[**]*Very abundant in tower vicinity.*
All others occur infrequently.

CPER was 0.55 (Knight 1972). Peak LAI was reached about mid-June and from 60% to 80% of total LAI was blue grama. In 1971 the greatest LAI increment occurred between April 20 and June 15, with a steady decline after June 15. This seasonal pattern of total LAI production for steppe vegetation was similar to the pattern of total amounts of chlorophyll (Rauzi and Dobrenz 1970). Patterns similar to these can be expected for any year, but the rate, time, and amount of LAI or chlorophyll production for a given year will reflect different precipitation and vegetation patterns. For example, the LAI production in the vicinity of the Pawnee Project meteorological tower may have a bimodal peak because of the frequent needleandthread in addition to the dominant blue grama.

Standard meteorological data has been gathered by CSU within the 6-ha grazing exclosure for several years. In addition, the exclosure includes a 8-m² weighing soil lysimeter. Seventy percent of the 311 mm of mean annual precipitation occurs between April and September. This low rainfall, generally flat to gently rolling terrain, the absence of local air pollution sources, along with the long-term meteorological data records, make it a good site for attempting to measure dry deposition.

The exclosure site described above is also a pollutant deposition research facility hosting three separate acid deposition monitoring programs:

1. National Atmospheric Deposition Program/National Trends Network (NADP/NTN). Wet and dry deposition chemistry measurements are collected and analyzed at a central NADP laboratory in Champaign, IL. Data from
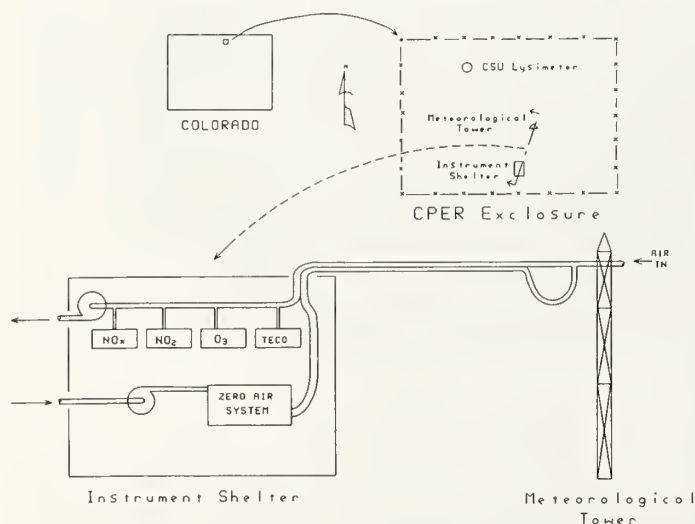

Figure 1.—Site location and vertical cross section of the instrument shelter, chemical instruments, and meteorological tower.

this site (NADP site no. 06222) are available from March 1978 to present.

2. NOAA/ATDD Dry Deposition Inferential Monitoring (DDIM). This site is no. 11 of the NOAA/ATDD core dry deposition sites. Filter-pac chemical analyses of site samples collected during the same sampling period and frequency as the NADP/NTN wet chemistry samples are conducted by the USGS laboratory in Atlanta, GA. Dry deposition chemistry is coupled with micrometeorological data to infer dry acid species fluxes (Hicks et al. 1985). Dry deposition chemistry and associated meteorological data are available from July 1986 to present.

3. USFS/RMFRES, Atmospheric Deposition Research Project, Pawnee Eddy Correlation Acid Deposition Research Site. Ambient air concentrations and eddy flux measurements of NO_2, NO_x, ozone, heat, and momentum have been collected during two short-term data collection periods from mid-December 1986 through January 1987 and from mid-May 1987 through July 1987. This last program is the subject of this paper.

Our eddy correlation system requires simultaneous measurements of the fluctuations in the vertical wind speed, heat, and chemical concentrations. These measurements are made at a rate between 10 and 20 Hz. Hence, both the wind sensor and chemical sensors must have relatively short response times (see appendixes A and B for a discussion of response times). Meeting these fast response time requirements requires very sensitive meteorological sensors and chemical analyzers. The chemical analyzers for this measurement program were provided by the University of Denver (appendix A). These instruments are housed in an instrument shelter, and ambient air was brought to them using a high-volume sample pump and a large-bore Teflon tube. A more detailed description of these sensors is given in appendix A and by Ray et al. (1986), Wendel et al. (1983), and Wesely et al. (1982). Table 2 lists the sensing instruments and analyzers integrated into the overall eddy correlation program.

During the two field periods, all eddy correlation measurements were made using a 3-axis Gill propeller anemometer for wind velocity and velocity fluctuations, and a fast response platinum resistance thermometer for temperature fluctuations. The Gill anemometer was corrected in real-time for non-cosine response (Massman and Zeller 1988). During one short test period in December 1986, a one-dimensional sonic heat flux sensor was used to compare heat fluxes acquired with the Gill anemometer and the fast response platinum resistance thermometer. We also plan to replace the Gill anemometer in future experiments with a 3-axis sonic anemometer.

Data collection and processing were accomplished using a personal computer interfaced with an analog-to-digital conversion board. Eight channels are available on the board for data acquisition and all eight channels (table 3) were sampled at ca. 14 Hz. Output measures include means, variances, covariances, and other micrometeorological parameters as listed in table 3. The software used for real-time data processing was adapted from McMillen's (1986) basic flux program for eddy correlation in nonsimple terrain. The compiled basic program is capable of running the entire eddy correlation measurement system unattended for several days. Tasks accomplished in real-time by this program include real-time data acquisition and processing, raw data storage if required, statistical summaries at the end of the assigned averaging period (usually 1/2 hour), instrumen-

Table 2.—Instrumentation used at Pawnee Acid Deposition Research Site for eddy correlation measurements.[a]

Instrument or model	Type	Parameter	Response time	Range
NO_x analyzer	chemiluminescence	NO_x	0.9 s	0.07 ppb – 1000 ppm
CAAM 2	chemiluminescence	NO_2	0.7 s	0.1–1000 ppb
CAAM 1	chemiluminescence	O_3	0.7 s	0.2–400 ppb
TECO 49	UV adsorption	O_3	2 min	1–500 ppb
R.M. Young UVW	Gill propeller anemometer	wind velocities	(b)	0.3–30 m/s
AIR, Inc.	platinum resistance	temperature	(b)	–50–+50 °C
Atmos. Tech. Inc.	3-axis sonic	wind velocities	(b)	0–20 m/s
Campbell Scientific	vertical sonic (CA27T)	heat flux		± 16 °C/ ± 4 m/s
AT&T 6300 +	PC computer (80286)	data collection and processing	--	--
Data Translations, Inc.	DT2805 board	A/D conversion	--	--

[a]*The use of trade and company names is for the benefit of the reader; such use does not constitute an official endorsement or approval of any service or product by the U.S. Department of Agriculture to the exclusion of others that may be suitable.*
[b]*See appendix B.*

3

Table 3.—Data acquisition and measured parameters at Pawnee Acid Deposition Research Site.

Channel	Parameter	Output (every 1/2 hr)
1	w: vertical wind speed	$\overline{w}$, $\overline{w'^2}$
2	u: horizontal wind speed component	$\overline{u}$, $\overline{u'^2}$
3	v: horizontal wind speed component	$\overline{v}$, $\overline{v'^2}$
4	T: temperature	$\overline{T}$, $\overline{T'^2}$
5	O_3 (Teco 49): ozone	$\overline{O_3}$, $\overline{O_3'^2}$
6	O_3 (CAAM1): ozone	$\overline{O_3}$, $\overline{O_3'^2}$
7	NO_2 (CAAM2): nitrogen oxide	$\overline{NO_2}$, $\overline{NO_2'^2}$
8	NO_x (nitrogen oxide)	$\overline{NO_x}$, $\overline{NO_x'^2}$
*	Momentum flux	$\overline{w'u'}$, $\overline{w'v'}$
*	Heat flux	$\overline{w'T'}$
*	Ozone flux	$\overline{w'O_3'}$
*	NO_2 flux	$\overline{w'NO_2'}$
*	NO_x flux	$\overline{w'NO_x'}$
*	Horizontal wind speed	$(\bar{u}^2 + \bar{v}^2)^{1/2}$
*	Wind direction	$\arctan(v/u)$
*	Friction velocity	$(-\overline{w'u'})^{1/2}$
*	Drag coefficient	$(-\overline{w'u'})/\bar{u}^2$
*	Horizontal wind rotation angle	η
*	Vertical wind rotation angle	θ
*	Sample frequency	n_s
*	# of samples/sample period	N

*Derived from data recorded on first 8 channels.

tation zero each half hour to ensure accurate chemical measurements, and instrument span calibration each half hour (not yet physically implemented).

The physical layout of the eddy correlation site is shown in figure 1. The relative directional location of the instrument shelter site to instrument tower was based on meteorological data collected during 1972–75, which showed the 210° azumuth as one of the least likely wind directions (Peterson and Parton, undated). However, the analysis of one year of 10-m-height wind data at the Pawnee Project tower (fig. 2) clearly shows that during daylight hours southerly wind directions dominate over all others, quite unlike what was expected from the 1972–75 data set.

Figure 2.—Pawnee site: a, annual wind rose; b, daytime, growing season wind rose.

EDDY CORRELATION SYSTEM ERRORS

Our dry deposition eddy correlation system employs a variety of instruments and support equipment; still, no data system is without sources of error. For example, Businger (1986) reviews and comments on several recent attempts by various researchers to measure dry deposition of gases and particles. He notes that up to the present there has been no discipline among the various researchers to ensure that their data have all the ingredients for an accurate determination of dry deposition, and he presents 10 specific sources of error that he claims are found in most field programs:

1. Failure to account for the effect of heat and water vapor fluxes;
2. Sampling errors due to insufficient averaging time;
3. Inadequate sensor response characteristics;
4. Sensors separated by too great a distance;
5. Random noise not accounted for;
6. Errors inherent in the horizontal uniformity and steady-state assumptions due to entrainment, advection, and nonstationarity;
7. Errors due to wrong sampling height;
8. Inadequate fetch;
9. Errors related to deliquescences of particles;
10. Errors due to flow distortion around sampling probes and mounting structures.

In order to make routine measurements of dry deposition fluxes, it is necessary to examine these and other errors and, where possible, account for them in the resulting data. We begin by examining errors that can
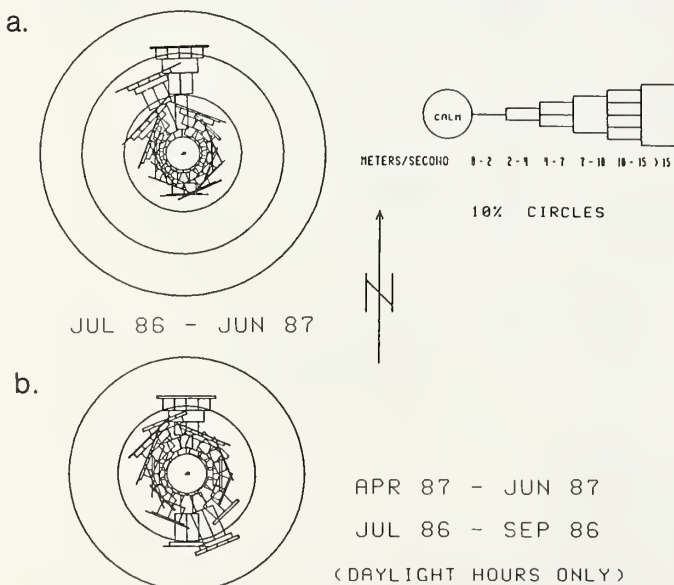
arise from sensor limitations in size and response, and instrument separation and mismatch.

Flux Loss Corrections

Methods similar to those of Moore (1986), as detailed in appendix B, were used to estimate the flux losses with the Gill propellers in the sensor array and then the data were corrected for these errors. The heat, momentum, and chemical flux losses for stable and unstable atmospheric conditions as a function of wind speed are given in figures 3, 4, and 5, respectively. The solid lines assume matched sensors and the dashed lines on these figures assume mismatched sensors (if no dashed line appears then sensor mismatch was not significant). By matched sensors we mean that the two separate types of instruments used to make the flux measurements have identical response characteristics and mismatched sensors mean they do not. The separation distances used for these computations were 36.0 cm between the vertical Gill propeller and the temperature sensor, 63.0 cm between the vertical Gill propeller and the horizontal Gill
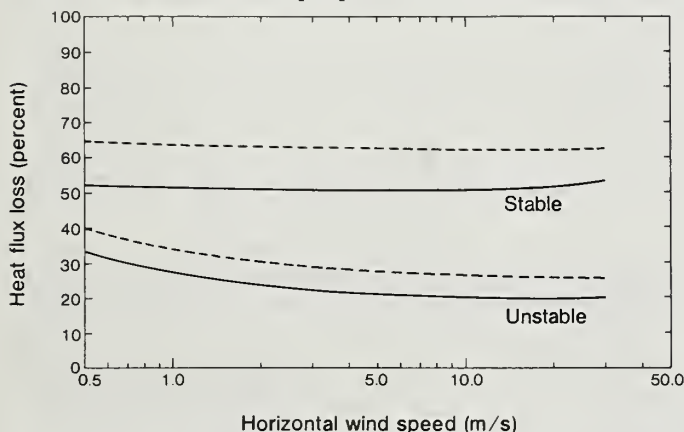
Figure 5.—Estimates of chemical flux loss as a function of wind speed and atmospheric stability associated with using the Gill propeller anemometer for measuring the vertical velocity fluctuations. Solid lines assume matched sensors; dashed lines assume mismatched sensors.

propellers, and 37.8 cm between the vertical Gill propeller and the mouth of the intake tube leading to the chemical sensors. For matched sensors, this system will underestimate the heat flux by at least 20% to 30% for unstable conditions and about 50% for stable conditions. Likewise, the momentum flux is underestimated between about 10% and 60%, depending upon wind speed and stability. These latter results are quite consistent with Horst's (1973b) estimates of the momentum flux loss that can be expected with Gill propellers. Finally, the ozone, NO_2, and NO_x flux losses are between 30% and 90%, again depending upon stability and wind speed. The NO_x flux loss is slightly higher than that of the other two sensors because of its slightly slower response time. These large flux losses result from the slow response times for both the Gill propeller and the chemical sensors.

The dotted lines on figures 3 and 5 give the estimates of the heat flux losses and the chemical flux losses caused by mismatching. For the heat flux, mismatching can increase the flux loss by another 8% for an unstable atmosphere and another 15% for a stable atmosphere. For the chemical fluxes, at low wind speeds the estimates of flux losses are also increased. For a stable atmosphere the flux loss is an additional 8% for the chemical fluxes, and for an unstable atmosphere it is about another 5%. As figure 5 also shows, mismatching has little effect on the chemical fluxes at moderate wind speeds, because the vertical Gill propeller has a response time comparable to that of the chemical sensors. Furthermore, this figure also shows that as the wind speed increases, mismatching again begins to contribute additional errors because of the reduction of the response time of the vertical Gill propeller at high wind speeds relative to the response time of the chemical sensors. Similar comparisons were made for the momentum flux losses. However, the response times of the horizontal and vertical Gill propellers were not different enough to introduce any significant mismatching errors.

In addition to the above errors associated with the Gill UVW, two other matters relating to its use for estimating

Figure 3.—Estimates of heat flux loss as a function of wind speed and atmospheric stability associated with using the Gill propeller anemometer for measurements of the vertical velocity fluctuations. Solid lines assume matched sensors, dashed lines assume mismatched sensors.
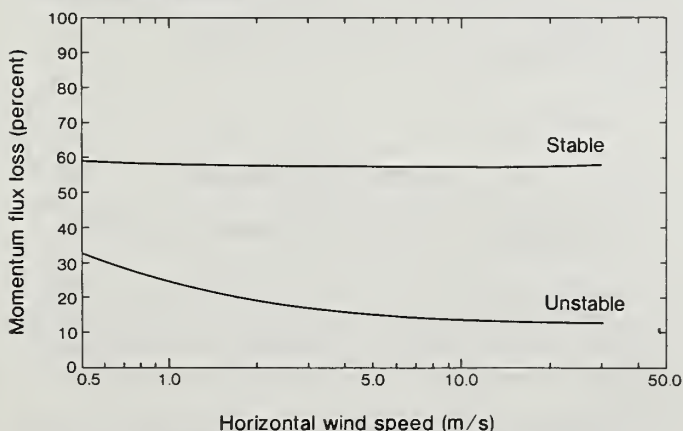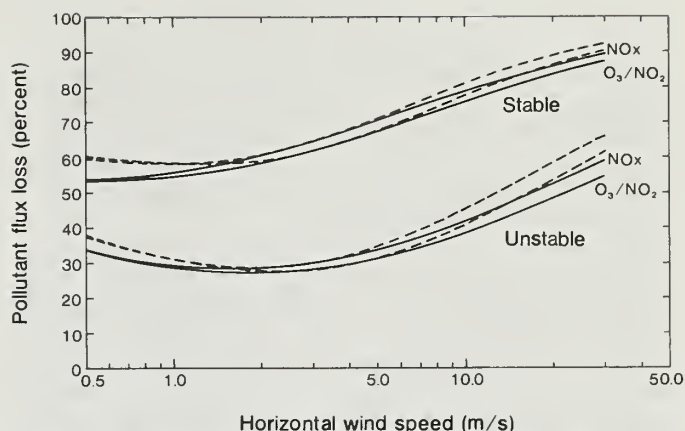
Figure 4.—Estimates of momentum flux loss as a function of wind speed and atmospheric stability associated with using 3-axis Gill propeller anemometer system for measuring the fluctuating velocity components.

5

turbulent fluxes and variances are relevant. The first involves the need to correct the turbulence data gathered with these instruments for their lack of a perfect cosine response. Massman and Zeller (1988) discuss this at length and provide an algorithm that can be used to make this correction in real-time. They show that without this correction, turbulent heat and momentum fluxes are underestimated by about 30%.

Unfortunately, the second problem cannot be fully corrected. Because these propellers tend to stall whenever the flow is greater than about 88° off axis, they will always underestimate turbulent fluxes. This is most serious with the vertical propeller, which senses a field that is always fluctuating through the propeller's stall region. This problem will be most severe whenever the horizontal velocity is significantly greater than the vertical velocity. Finkelstein et al. (1986) discuss in greater detail the limitations of these sensors for turbulence measurements.

Again, the methods outlined in appendix B were used to estimate the flux loss errors associated with using the 3-axis sonic anemometer in place of the Gill anemometer. For this case, the separation distances are 6.35 cm, 0.0 cm, and 30 cm between the center of the vertical sonic's acoustic path and the temperature sensor, the center of the acoustic path of the horizontal sonic, and the mouth of the intake tube to the chemical sensors, respectively. The solid curves and dashed curves of figures 6, 7, and 8 give the results of the computations for the flux losses for the sonic anemometer corresponding to figures 3, 4, and 5, respectively. In general, the 3-axis sonic anemometer provides much better estimates of the fluxes of heat and momentum at all wind speeds and the fluxes of the three chemical species at low wind speeds than does the Gill anemometer. Figures 6 and 7 show that the sonic anemometer will probably underestimate heat and momentum fluxes by about 5% to 30%, and figure 8 shows that the fluxes associated with the three chemical species will be underestimated for wind speeds below about 7 m/s between 20% or 30% to 60%, depending upon stability. At wind speeds above 7 m/s, there is little improvement in the estimates of the fluxes of O_3, NO_2, and NO_x with the sonic anemometer over the Gill anemometer; this is largely a reflection of the nature of the chemical sensors and their characteristics and is quite independent of the nature of the vertical velocity sensor.

The dotted curves of figure 8 also show that the mismatching of these two types of sensors can introduce an additional 5% to 10% underestimation of the chemical fluxes, depending upon atmospheric stability and wind speed. A similar computation for the heat flux measurements showed that the mismatching errors associated with the temperature sensor and the vertical sonic anemometer were negligible.

It is also important to note that at higher wind speeds the mismatch between the sonic anemometer and the chemical sensors is actually worse than it is between the Gill propeller anemometer and these chemical sensors. Consequently, there is a greater loss of flux at higher wind speeds when using a sonic anemometer to measure
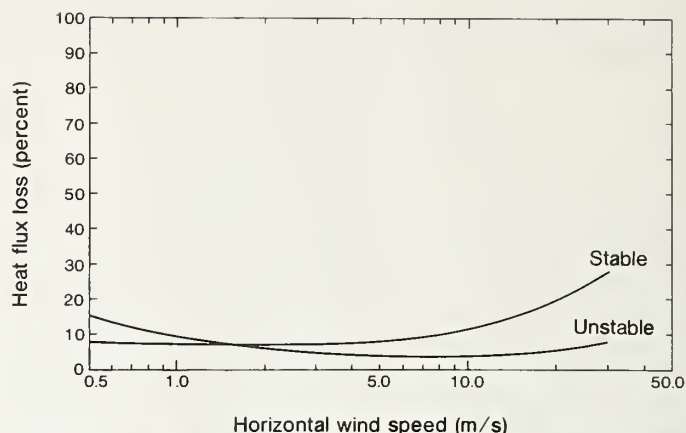

Figure 6.—Same as figure 3 except for the use of a sonic anemometer rather than the Gill propeller anemometer.
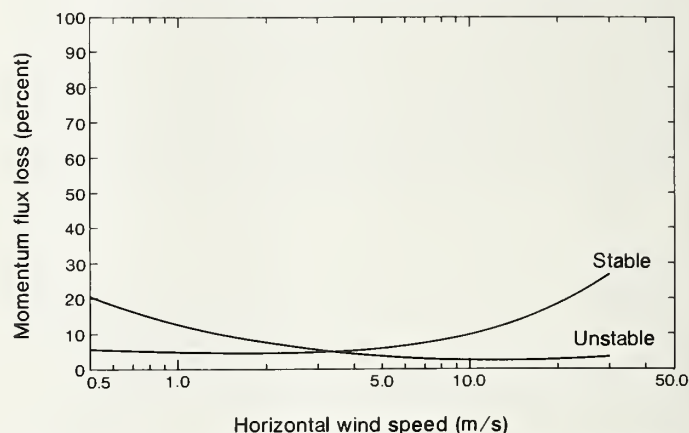

Figure 7.—Same as figure 4 except for the use of the 3-axis sonic anemometer rather than the 3-axis Gill propeller anemometer.
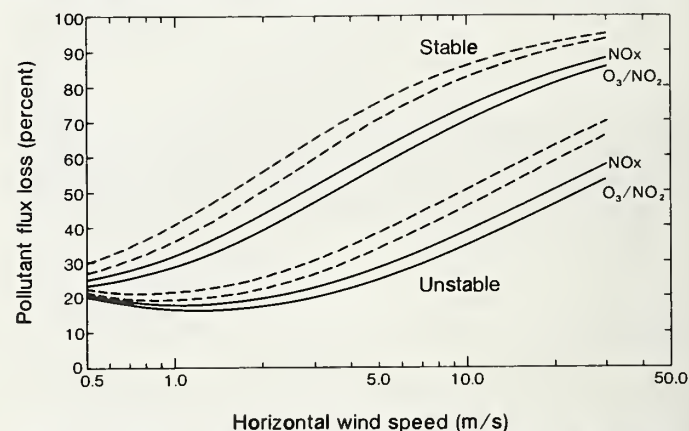

Figure 8.—Same as figure 5 except for the use of the sonic anemometer rather than the Gill propeller anemometer.

the fluctuating component of the vertical velocity than when using a Gill propeller anemometer. For correcting our flux measurements, we assume the instruments are mismatched and use the dashed curves in figures 3, 5, and 8.

Although it is important to use the results from these figures to correct turbulence data obtained with the sonic anemometer, it is also important to correct the data for shadowing effects. Shadowing will cause the measured

velocity component to be underestimated because of partial shadowing of the acoustic path by the tranducers. We plan to use the algorithm being developed by Conklin et al. (1988) for this correction to the 3-axis sonic anemometer.

In addition to comparing and correcting flux estimates derived with the Gill and sonic anemometers, other aspects of sensor performance were considered. One was the relative importance of the volume averaging effects that the intake tube of the chemical sensors can have upon the estimates of the flux loss. These volume averaging effects arise because measurements of concentration are not made at a point, but rather such measurements represent the average concentration of a finite volume of air that has been drawn into the chemical sensors through the Teflon tube. To assess these effects, estimates of the O_3, NO_2, and NO_x flux losses with and without the response function appropriate to volume averaging (appendix C) were needed for both types of anemometers. Volume averaging effects were shown to be negligible in both cases. Therefore, the major reason for the significant losses of O_3, NO_2, and NO_x fluxes (figs. 5 and 8) is largely the slow response times of these sensors.

Variance Loss Corrections

In addition to the flux loss correction, the variance loss for the sensors was also estimated. Appendix B gives the details of the computations used in the following discussion.

The variance loss estimate for temperature, vertical velocity (for both the Gill and sonic anemometers) and the chemical species are presented in figures 9–12. The conclusions that can be drawn from these figures are the same as with the flux loss estimates; namely, (1) that the sonic anemometer generally represents an improvement over the Gill propeller anemometer, and (2) that the slow response of the chemical sensors can cause significant losses to the variance measurements, especially for stable conditions. However, there is one important difference between these variance loss estimates and the preceding flux loss estimates. In many cases, the variance loss is explicitly dependent upon the stability parameter z/L, as discussed in more detail in appendix B. This is always true whenever the atmosphere is stable, and it is true for the vertical velocity variance for unstable conditions as well. For the flux loss estimate, on the other hand, it is sufficient to know only whether the atmosphere is stable
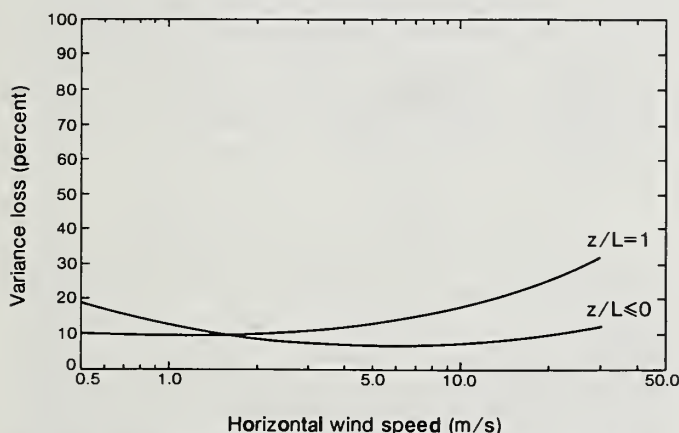

Figure 9.—Estimates of temperature variance loss with the fast-response platinum wire resistance thermometer as a function of wind speed and atmospheric stability.
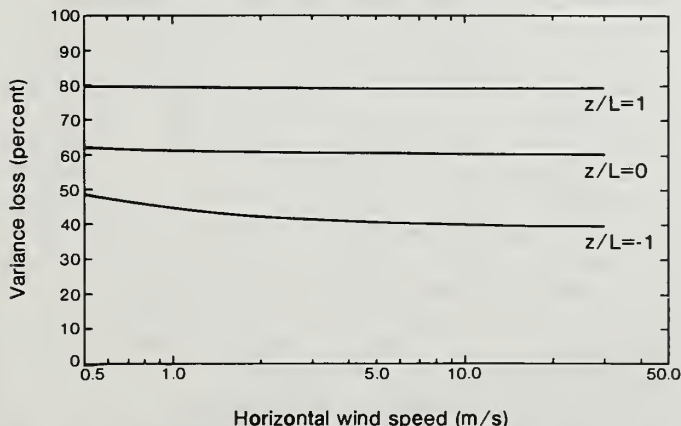

Figure 10.—Estimates of vertical velocity variance loss with the Gill propeller anemometer as a function of wind speed and atmospheric stability.
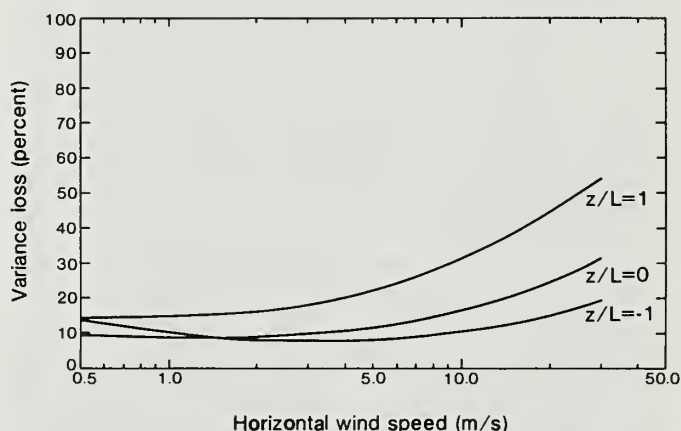

Figure 11.—Estimates of vertical velocity variance loss with a sonic anemometer as a function of wind speed and atmospheric stability.
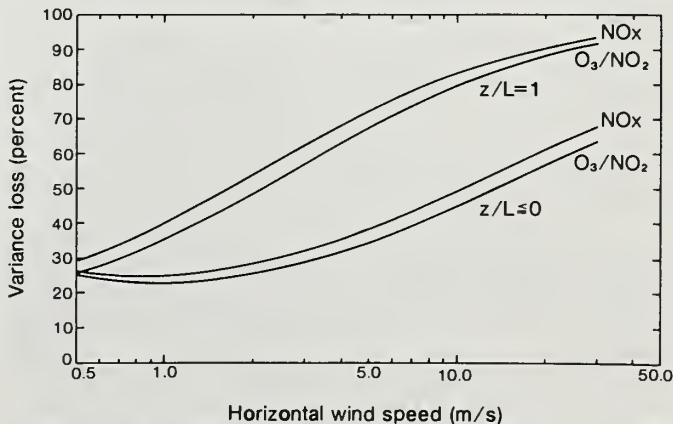

Figure 12.—Estimates of variance loss from O_3, NO_2, and NO_x measurements as a function of wind speed and atmospheric stability.

7

or unstable (equivalent to knowing only the sign of z/L or the direction of the heat flux). Therefore, in order to correct for any loss of variance, we must first correct for any loss of heat and momentum flux using the estimates derived above; next we compute a value for z/L based on the heat and momentum fluxes; and then we make an estimate of variance loss for that value of z/L. Obviously, estimating the variance loss is considerably more complicated than for estimating flux losses.

Finally, an important caveat must be stated concerning all estimates of the flux or variance losses. There is some uncertainty in the atmospheric spectra and cospectra used for these computations [see Moore (1986) for further discussion]. Although this uncertainty is not serious for small estimates of loss (less than about 30%), it can become more important at higher estimates of loss, which can make the correction less reliable whenever the flux loss is large.

Additional Sources of Errors

In addition to the errors associated with instrument response, size, and siting geometry, outlined above, it is equally important to be aware of and account for other important measurement limitations and problems associated with the eddy correlation technique. For example, both heat and moisture fluxes can significantly influence flux measurements (Webb et al. 1980), as can digitization noise (Kristensen and Kirkegaard 1987), random uncorrelated noise (Lenschow and Kristensen 1985), flow distortion effects (Wyngaard 1988, Högström 1988), and site inadequacies such as insufficient fetch and lack of surface uniformity.

Corrections to dry deposition fluxes due to heat and moisture fluxes arise because of the atmospheric density variation associated primarily with the heat flux and secondarily with the moisture flux. For our site the humidity is low and much of the time evapotranspiration (moisture flux) is not large; therefore, we will use the following expression for correcting the measured fluxes of O_3 and NO_2:

$$F = F_m + (\bar{\rho}_c \overline{w'T'})/\overline{T} \qquad [1]$$

where F_m is the measured flux after the instrument corrections outlined in the previous section have been applied, $\bar{\rho}_c$ is the mean concentration of the constituent (O_3 or NO_2), $\overline{T}$ is the mean ambient temperature, and $\overline{w'T'}$ is the heat flux also measured after the instrument corrections have been applied. Our experience has shown that the correction term $(\bar{\rho}_c \overline{w'T'})/\overline{T}$ in this equation is typically between 1% and 20% of the measured ozone flux and is frequently significantly higher for the measured NO_2 fluxes. The NO_x sensor, on the other hand, does not require this correction. Fundamentally this sensor measures the mixing ratio rather than a concentration as do the ozone and NO_2 sensors. For measurements of fluxes based upon mixing ratios, Webb et al. (1980) have shown that no correction need be applied.

In the case of variance measurements, digitization noise can also influence measurements (Kristensen and Kirkegaard 1987). Although a correction for this effect was included in our data analysis, usually it was negligible.

Uncorrelated noise (Lenschow and Kristensen 1985) can also impact flux measurements. This is particularly true whenever the instruments are event counters. Our chemical sensors measure a current rather than counting photons, and the concentrations being measured are sufficiently high that this type of uncorrelated noise error does not contribute significantly to our errors.

Flow distortion effects caused by sensor geometry and their positioning on towers can also influence observations significantly (Wyngaard 1988, Högström 1988). Our measurements are undoubtedly influenced to some extent by these effects; however, drawing air samples into the shelter with an intake tube minimizes the amount of equipment placed on the towers, which should considerably reduce flow distortion effects.

Finally, patchiness in the local vegetation cover and inadequate fetch can also interfere with flux measurements; but, these site limitations do not appear at present to have had any significant impact on our data. (We say this because, as will be shown in the next section, our data agree with previously and independently made observations.) However, eddy correlation measurements of moisture flux and independent measurements of the surface energy balance are planned and should provide more insight into how much site limitations (and flow distortion as well) can influence the data.

DATA RESULTS AND ANALYSIS

Sample results from our Pawnee program were used to assess the utility and performances of the different meteorological and chemical sensors. To examine normalized variances of temperature and vertical velocity and the correlation coefficient between temperature and vertical velocity, the Monin-Obukhov similarity theory was used. Similar computations were performed for the ozone, NO_2, and NO_x fluxes. Deposition velocities and surface resistances derived from our system at the Pawnee site were compared with similar measurements made at other sites for these three acid species.

For this analysis, we selected a 2-week period beginning on June 30, 1987, at 9:00 a.m. MST, which made available a set of more than 600 potentially useful data points (fluxes, variances, etc.) at half-hour intervals. As an example of these data, figures 13, 14, and 15 give the corrected heat, momentum, and ozone fluxes, respectively, for the week beginning with June 30. These data have not been smoothed or checked for bad data points (discussed below), and breaks in the curves occur whenever data were not recorded. However, not all these data are useful, and the following criteria were developed for limiting the analysis to the best data.

1. Data taken when the wind direction was between 150° and 225° were eliminated. This precluded any interference by the tower and the instrument shelter on the measurements.

2. Data taken when the horizontal wind speed was less than about 1.9 m/s were also eliminated. This criterion was necessary to ensure that the anemometry would resolve the momentum flux adequately. The exact value of this cutoff wind speed was determined by trial and
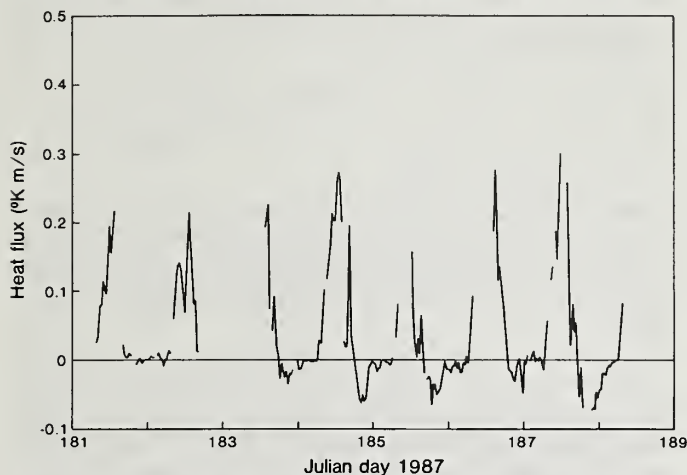

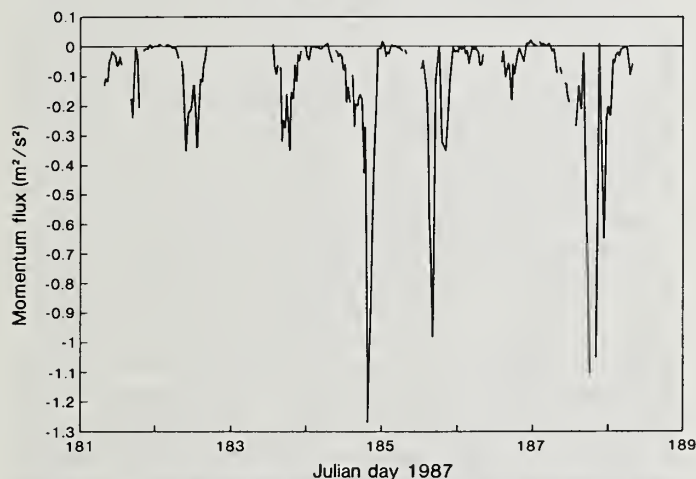Figure 13.—Corrected heat flux for week beginning June 30 (day 181).

Figure 14.—Corrected momentum flux for week beginning June 30 (day 181).
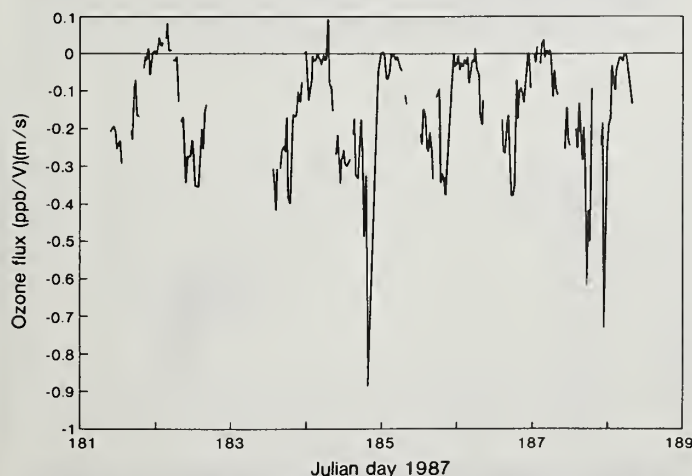

Figure 15.—Corrected ozone flux for week beginning June 30 (day 181).

error and resulted from an analysis of the roughness length appropriate to our site, as is discussed more fully later.

3. All momentum flux measurements larger than -0.0025 m²/s² were also eliminated. The purpose here was to remove all positive momentum fluxes and all small negative stresses that are below the instrumentation's ability to resolve. Contrary to expectations, the observed momentum flux is sometimes positive, possibly because of the brief and intense "bursts," which in the atmospheric boundary layer have been observed to reverse the sign of the momentum flux (Haugen et al. 1971). These positive momentum fluxes were removed because all computations involving Monin-Obukhov similarity theory and surface roughness lengths require negative Reynolds stress only.

4. All time series (temperature, velocities, chemical concentration, fluxes, etc.) were visually checked and all obviously noisy data points were removed. These data were usually in the form of individual spikes in the data and were simply unrealistic on physical grounds. (Examples of this type of data would include ambient temperature measurements that exceed the boiling point of water.)

5. For the analysis of the NO_2 and NO_x data, our criterion required that the observed NO_x concentration exceed the observed NO_2 concentration (otherwise the data from both sensors were eliminated). In a few instances, the observed NO_2 concentration did exceed the observed NO_x concentration. In some cases, this was due to low or nonexistent flow rates of the chemiluminescent reactant through the reaction chamber; in other cases, however, this discrepancy was not fully understood but may have been due to problems in the calibration of these two sensors.

6. All data referring to the fast response chemical sensors taken during periods of calibration of the chemical instruments were eliminated. During a calibration period (usually twice weekly), the instruments were manually being adjusted and tested; hence the data recorded by the computer system during this time will not reflect ambient conditions. A calibration of these instruments typically requires between 30 and 60 minutes.

Employing these six criteria reduced the total number of acceptable data points from a potential of more than 600 to between 200 and 300, depending on what parameter was being analyzed.

Site Roughness and Monin-Obukhov Similarity Theory

Wind speed above a surface is influenced by the momentum flux, the surface roughness length, and the atmospheric stability. The relationship between these variables is defined as follows:

$$\bar{u} = \frac{u_*}{k}[\ln(z/z_o) - \psi_m(z/L)] \qquad [2]$$

where ψ_m is the atmospheric stability influence function for momentum, z_o is the surface roughness length, z is the instrument height (6 m), k is the von Karman con-

stant, and u_* is the friction velocity defined as $(-\overline{u'w'})^{1/2}$ where $-\overline{u'w'}$ is the Reynolds stress.

The influence function, ψ_m, is generally expressed as follows (Paulson 1970, Businger et al. 1971):

$$\psi_m(z/L) = \begin{cases} 2\ln\left(\dfrac{1+x}{2}\right) + \ln\left(\dfrac{1+x^2}{2}\right) - \tan^{-1}x + \pi/2 \\ \qquad\qquad z/L \leq 0 \text{ (unstable, neutral)} \\ -5\,z/L \qquad z/L > 0 \text{ (stable)} \end{cases} \quad [3]$$

where $x = (1 - 16\,z/L)^{1/4}$.

Therefore, using our measurements of heat and momentum fluxes, wind speed, and temperature and employing the corrections outlined in the previous section, we could compute z_0 with the above relationships. Figure 16 shows the computed values of roughness length plotted against wind speed for our data set for all wind speeds greater than 1.9 m/s. Except for one outlier ($z_0 \approx 45$ cm, $\overline{u} \approx 3$ m/s), all roughness lengths are between about 0.5 and 30 cm. The reason 1.9 m/s was chosen as the lower cutoff speed for acceptable measurements is that all other outliers were associated with these lower wind speeds and not with wind direction. Therefore, it was concluded that our data system could not resolve momentum flux at wind speeds below about 1.9 m/s.

The average z_0 computed from the data shown in figure 16 is 4.2 cm $\pm$ 5.0 cm, a value in good agreement with the 4 cm found by Korrell et al. (1982) for most wind directions at the Boulder (Colorado) Meteorological Tower which is located about 100 km southwest of our site in similar terrain with similar plant cover. However, our results, unlike theirs, did not show any correlation between z_0 and wind direction, although with our 6-m measurement height our z_0 values are probably influenced by local terrain features.

In addition to the large variability in our z_0 values, it is also important to examine other effects that may lend further uncertainty to defining a z_0 value for our site. Both the form chosen for ψ_m and any systematic underestimation of the momentum flux can cause z_0 values to differ significantly from those shown in figure 16. For example, the results presented by Carl et al. (1973) yield a different form for ψ_m appropriate to unstable at-

mospheric conditions; and, Högström (1988) found, when correcting [3] for flow distortion errors, that for unstable condition $x = (1-15.2\,z/L)^{1/4}$ and for stable conditions $\psi_m(z/L) = -4.8\,z/L$. These two corrections resulted in a better representation of $\psi_m(z/L)$ than [3]. The results of Carl et al. (1973) produce the following expression for unstable ψ_m:

$$\psi_m(z/L) = 3/2\,\ln\left(\frac{1+x+x^2}{3}\right) - \sqrt{3}\,\tan^{-1}\left(\frac{2x+1}{3}\right) + \pi/\sqrt{3}$$
$$z/L > 0 \quad [4]$$

where $x = (1-15\,z/L)^{1/3}$.

Using [4] instead of [3] yields z_0 values that are about 40% lower for unstable atmospheric conditions than those shown in figure 16, while Högström's formulation of [3] produced essentially negligible changes in the z_0 values.

Likewise, systematic underestimation of the momentum flux can also impact our z_0 computations. Such systematic errors can arise due to poor vertical alignment, degradation of the bearings in the Gill propeller, etc. We repeated our z_0 computations assuming that the momentum stress was consistently underestimated by 25% and found that all z_0 values were 50% higher than those shown in figure 16. Given these results and those concerning ψ_m and the variability in z_0 in general, we take $z_0 = 4$ cm for our site, but the uncertainty associated with this value is large. Finally, it should be noted that z_0 should vary with time of year and the nature of the plant cover or snow cover. Therefore, our z_0 value may be valid only for the present data set.

Monin-Obukhov similarity, in addition to providing some insight into the influence function, ψ_m, for our z_0 correlations, also predicts the functional relationships between z/L and the normalized variances of vertical velocity, σ_w^2/u_*^2, and temperature, $(-z/L)\sigma_T^2 u_*^2/(\overline{w'T'})^2$. Because these two normalized variances are combinations of various quantities measured by our system, computing them with our data provides (1) a method to assess the quality or information content of our data set and (2) a means for checking the correction factors derived in the previous section.

Figure 17 is a plot of σ_w^2/u_*^2 vs. z/L as computed with our data and as expected from similarity theory [solid
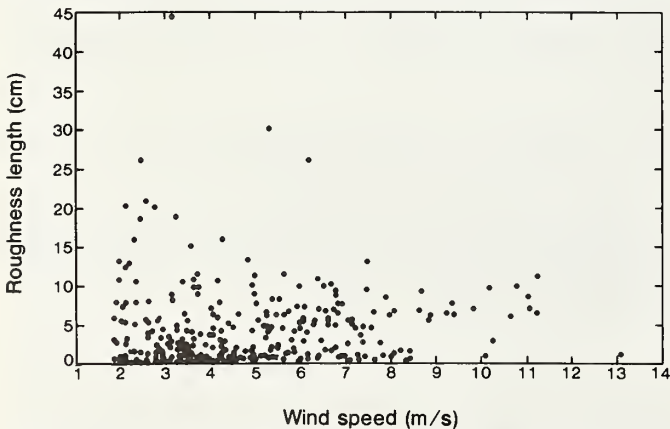
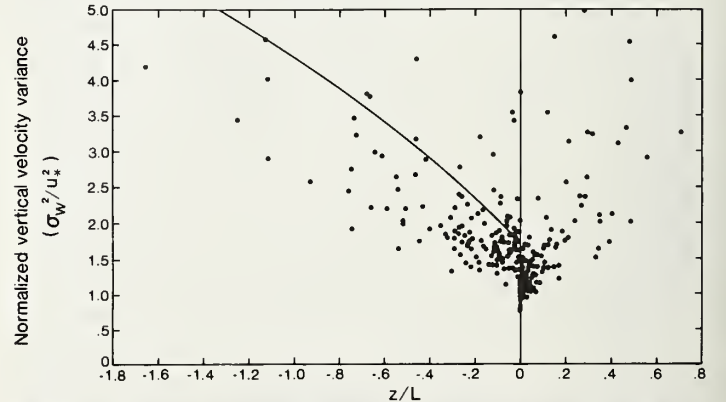Figure 16.— Roughness length vs. wind speed for the 2-week period June 30–July 14.

Figure 17.— Vertical velocity variance σ_w^2 normalized by u_*^2 vs. z/L. Observed data is given by •; similarity theory prediction is given by the solid line.

line = $1.7(1-3 z/L)^{2/3}$, from Panofsky et al. (1977)]. Although the individual data points obviously show significant variability, the data in some average sense appear to follow the expected curve. This suggests that the correction factors discussed in the previous section are realistic overall, but that they may be in error for individual points. This may arise in part from the assumption that the response length of the vertical Gill propeller is constant (appendix B); whereas, it is in fact a function of the wind velocity's angle of attack, which may vary from data point to data point. Some portion of the scatter shown in figure 17 is also probably due to errors in the measurement of the momentum flux. This is a particularly demanding measurement which is quite sensitive to even small errors in alignment and other effects. Finally, during stable atmospheric conditions ($z/L>0$), these difficulties are further compounded because (1) the fluxes and variances will usually be much smaller in magnitude than for unstable atmospheric conditions, placing greater demands on the instrumentation, and (2) the correction factors become less certain for stable conditions because the spectra and cospectra are themselves less well defined in stable conditions.

Figure 18 is a plot of $(-z/L)\sigma_T^2 u_*^2/(\overline{w'T'})^2$ vs. z/L as computed with our data and as expected from similarity theory (solid line = $0.92(-z/L)^{2/3}$, from Wyngaard et al. (1971). The agreement between our observations and similarity theory is better than in the previous figures and is actually surprisingly good except for a few points between $z/L = 0$ and $z/L = -1.5$. The reduction in scatter over the results in the previous figure may be due to the use of a relatively high-performance temperature sensor. Certainly fewer assumptions were involved in estimating variance and flux losses with this sensor than with the Gill propeller anemometer.

Figure 19 is a plot of the correlation coefficient, r_{wT} between temperature and vertical velocity vs. z/L. The correlation coefficient is defined as $\overline{w'T'}/(\sigma_w \sigma_T)$. This plot shows that in unstable conditions $r_{wT} \approx +0.55$, and for stable conditions $r_{wT} \approx -0.15$. However, the data possess a large amount of variability. For unstable conditions, our value of r_{wT} is in good agreement with Haugen et al. (1971). For stable conditions, however,
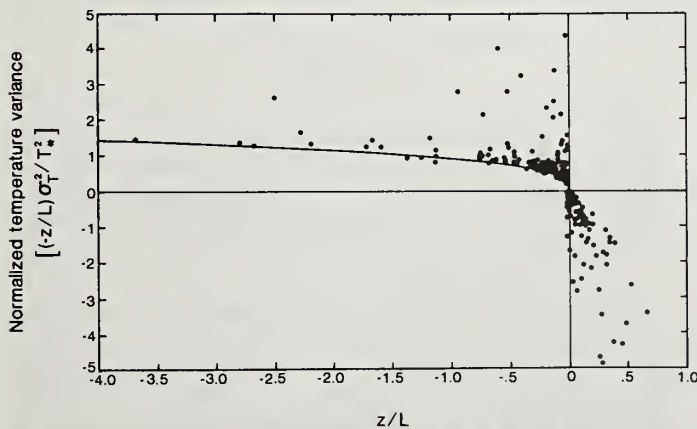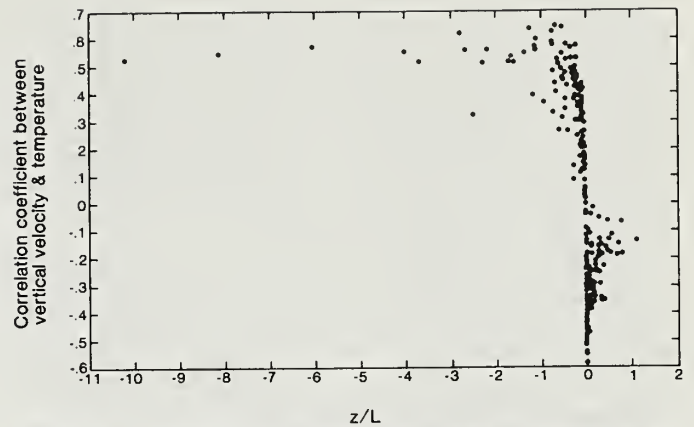
Figure 19.—Correlation coefficient between the fluctuations of vertical velocity and temperature vs. z/L for the 2-week period June 30–July 14.

Haugen et al. (1971) suggest that $r_{wT} \approx 0.3$. Again, this discrepancy could be the result of the many possible errors associated with these measurements during stable conditions.

Ozone

Up to now, we have simply assumed that ozone is transported and dispersed by atmospheric turbulence in a manner similar to temperature. However, comparing the normalized ozone variance $(-z/L)\sigma_{O_3}^2 u_*^2/(\overline{w'O_3'})^2$ against z/L, provides an important consistency check of this similarity assumption. Figure 20 is the same as figure 18 except for a different range of z/L values and the use of the ozone data rather than the temperature data. Although there is somewhat more scatter and fewer data points in figure 20 than in figure 18, the results are still quite similar. There is nothing, therefore, in either of these figures to invalidate our assumptions of similarity between these two atmospheric scalars.

The correlation coefficient between ozone and the vertical velocity, r_{wO_3}, can also provide some information concerning the utility of the variance method of esti-

Figure 18.—Normalized temperature variance vs. z/L for the 2-week period June 30–July 14. Observed data is given by •; similarity theory prediction is given by the solid line.
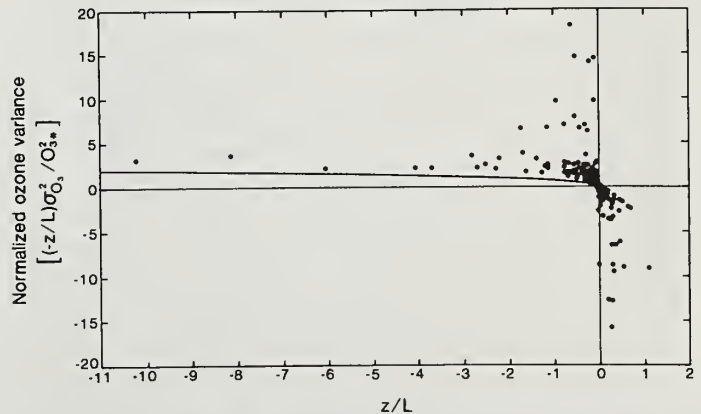
Figure 20.—Normalized ozone variance vs. z/L for the 2-week period June 30–July 14. Observed data is given by •; similarity theory prediction is given by the solid line.

mating the ozone flux (Businger 1986). From figure 21, which gives a plot of r_{wo_3} vs. z/L, r_{wo_3} can probably be approximated by a single value (–0.55) reasonably well. Although again these data show a lot of scatter, they are in good agreement with the r_{wT} for unstable conditions. However, for stable conditions all values between –0.1 and –0.6 seem to be about equally represented for r_{wo_3}. Thus, it is not possible to confirm or reject the usefulness of the variance method.

In addition to examining the ozone data using Monin-Obukhov similarity theory, we can also use this data to derive deposition velocities and surface resistances. The deposition velocity, v_d, is defined as the negative turbulent flux divided by the mean concentration; the surface resistance, r_s, is defined as follows:

$$r_s = \frac{1}{v_d} - \frac{1}{ku_*}\left[\ln(z/z_0) - \psi_c(z/L)\right] - \frac{2.63}{ku_*} \qquad [5]$$

where ψ_c is the influence function for ozone. Assuming that ψ_c is equal to the influence function for heat, we have (Paulson 1970):

$$\psi_c(z/L) = \begin{cases} 2\ln\left(\frac{1+x^2}{2}\right) & z/L \le 0 \\ -5\,z/L & z/L > 0 \end{cases} \qquad [6]$$

where $x = (1-16\,z/L)^{1/4}$. From the definition of surface resistance, [5], we see that it is a residual and equal to the total resistance, $r_t \equiv 1/v_d$, less the aerodynamic resistance, $([\ln(z/z_0) - \psi_c(z/L)]/ku_*)$, and the boundary layer resistance, $(2.63/ku_*)$. Further discussion of these latter two resistance terms can be found in Hicks et al. (1985).

Figures 22 and 23 give, respectively, the deposition velocities and the surface resistances for ozone as a function of the time of day for our data set. The mean deposition velocity for ozone is 0.43 cm/s and the range of our observed deposition velocities (about 0.1 cm/s to about 1.2 cm/s) are in good agreement with all other observations (e.g., Wesely et al. 1978; Sehmel 1980; Delaney et al. 1986). The surface resistance for ozone basically should reflect the behavior of the plant cover during the course of a diurnal cycle, which is roughly what figure
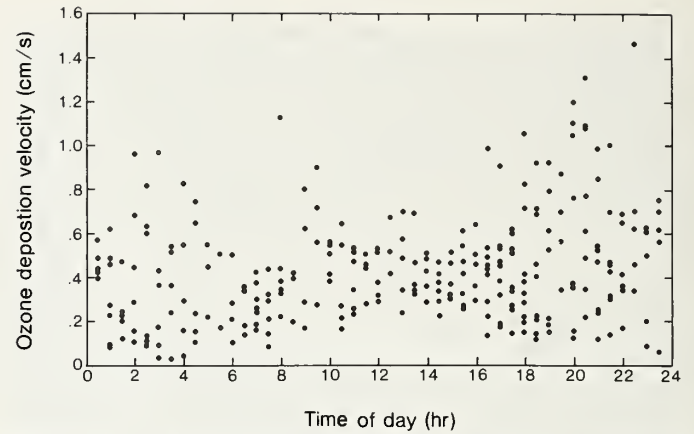

Figure 22.—Ozone deposition velocity as a function of time of day for the 2-week period June 30–July 14.
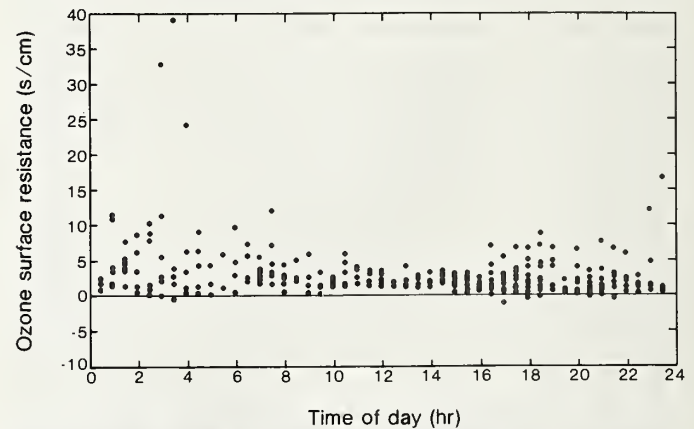

Figure 23.—Surface resistance to ozone uptake as a function of time of day for the 2-week period June 30–July 14.

23 shows. Although there is a lot of scatter in these data, generally higher resistances are seen at night and lower resistance in the daylight hours, with a minimum resistance between 2 and about 4 s/cm between about 900 hours and 1,600 hours and a maximum resistance between about 10 to 20 s/cm at other times during the day. This diurnal cycle of surface resistance, as portrayed in the figure, is in good agreement with the diurnal cycle of stomatal resistance for *Bouteloua gracilis* (Monson et al. 1986), the dominant plant in the area.

NO$_2$ and NO$_x$

The NO$_2$ and NO$_x$ data were analyzed in a manner identical to that discussed above for ozone and, inasmuch as the results and conclusions apply equally to both NO$_2$ and NO$_x$, only the NO$_2$ sensor will be discussed. The results for the NO$_2$ sensor are summarized in the next four figures.

Figures 24 and 25 give the measured NO$_2$ concentration (in ppb/volume) and corrected NO$_2$ fluxes for the first week of our data set. Both the NO$_2$ concentrations and the NO$_2$ fluxes are highly variable. The positive NO$_2$ fluxes in figure 25 indicate that the surface itself may be a source for NO$_2$, as has in fact been observed (Slemr and Seiler 1984, Williams et al. 1987). Further-
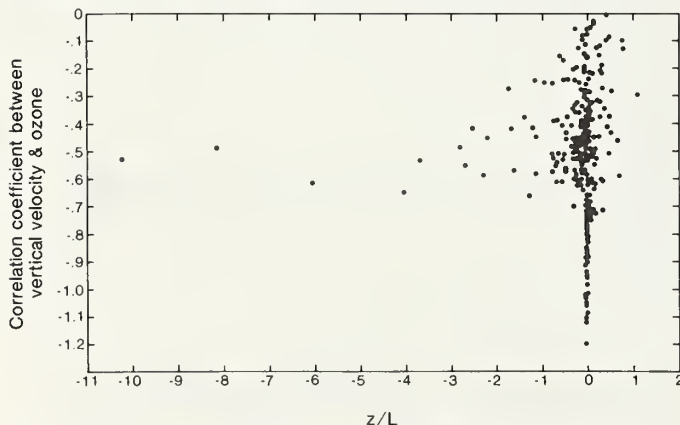

Figure 21.—Correlation coefficient between the fluctuations of vertical velocity and ozone concentration vs. z/L for the 2-week period June 30–July 14.
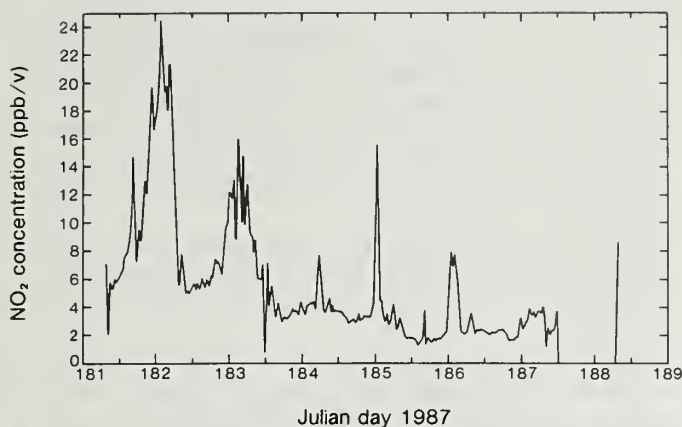
Figure 24.—NO_2 concentration as a function of time during the 1-week period June 30–July 7.

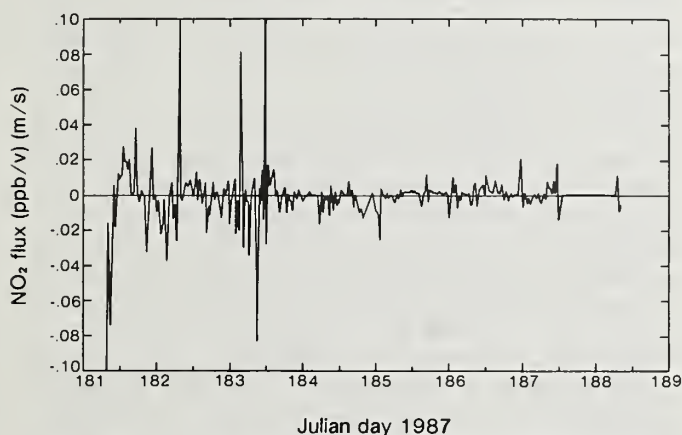Figure 25.—NO_2 flux as a function of time during the 1-week period June 30–July 7.

Figure 26.—Correlation coefficient between the fluctuations of vertical velocity and NO_2 concentration vs. z/L.

Figure 27.—NO_2 deposition velocity as a function of time of day for the 2-week period June 30–July 14.

more, the variability in the NO_2 source strength at the surface has also been observed to be extremely variable in both time and space. For example, Slemr and Seiler (1984) reported variation in source strength of over 100-fold. To further complicate the interpretation of our data, natural NO_x emitted from soils is oxidized in the presence of ozone and ultraviolet radiation to NO_2. When this occurs (which it certainly must at our site), Fitzjarrald and Lenschow (1983) and Lenschow and Delany (1987) have shown that the measured fluxes can be in error by significant amounts (about 30% at our measuring height of 6 m).

Figure 26 gives r_{wNO_2} as a function of z/L and figure 27 gives the NO_2 deposition velocity for NO_2 as a function of the time of day. In the first of these two figures, there is no clear evidence of any correlation between the vertical velocity fluctuations and the NO_2 concentration fluctuations. The deposition velocities clearly reflect the variability in the NO_2 flux itself.

Although our results are inconclusive for NO_2, it should be noted that our observations are very similar to other observations of NO_2 and NO_x measurements (e.g., Delaney et al. 1986, Hicks et al. 1986). In general, until more is understood quantitatively about the role of generation and destruction of NO_x and NO_2 at the surface and within the soil, it will be difficult to make further progress on interpreting similar measurements.

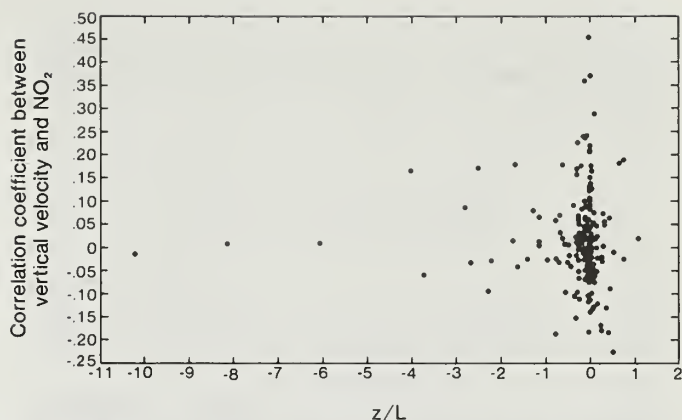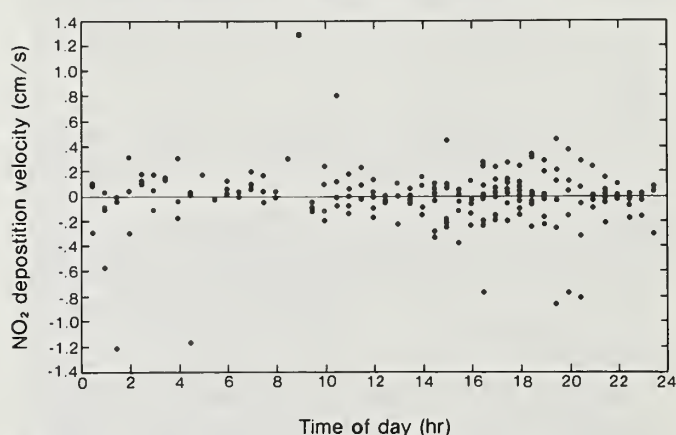Furthermore, it will probably require some sort of a soil nitrogen cycle model coupled with a chemical and atmospheric transport model to fully interpret our results.

SUMMARY

Our efforts at measuring the dry deposition fluxes of ozone, NO_2, and NO_x employing the eddy correlation method have been outlined. Although this method is demanding and complex, at present it offers the only direct approach available for making these measurements and, therefore, we chose this technique over any other. Although an attempt was made to account for as many errors associated with this approach as possible, sources of errors undoubtedly remain. Nevertheless, the results of our initial analysis suggest that our eddy correlation system produces realistic and valid data that agree with many previous and independent meteorological and biological measurements.

Finally, it should be emphasized that this report is part of a continuing effort at the Pawnee Grasslands. More detailed analysis of the data gathered to date is planned, and the system will be expanded to include moisture flux measurements using eddy correlation methods. Furthermore, long-term comparisons of the eddy correlation fluxes of heat and moisture with other independently

13

measured terms of the surface energy balance are also planned. Hopefully, these and other future plans should further demonstrate the utility and validity of our system and the quality of our site.

LITERATURE CITED

Anderson, D.E.; Verma, S.B.; Clement, R.J. [and others]. 1986. Turbulence spectra of CO_2, water vapor, temperature and velocity over a deciduous forest. Boundary-Layer Meteorology. 38: 81–99.

Andreas, E.L. 1981. The effects of volume averaging on spectra measured with a Lyman-Alpha hygrometer. Journal of Applied Meteorology. 20: 467–475.

Brock, F.V.; Nicolaidis, C.E. 1985. Instructor's handbook on meteorological instrumentation. NCAR/TN–237 + 1A, National Center for Atmospheric Research, Boulder, CO.

Brown, L.F.; Trlica, M.A. 1974. Photosynthesis of two important grasses of the shortgrass prairie as affected by several ecological variables. IBP Technical Report No. 244. 190 p.

Burkhardt, M.R.; Maniga, N.I.; Stedman, D.H. [and others]. 1988. Gas chromatographic methods for measuring nitrogen dioxide and peroxyacetyl nitrate in air without compressed gas cylinders. Analytical Chemistry. 60: 816–819.

Busch, N.E.; Christensen, O.; Kristensen, L. [and others]. 1980. Cups, vanes, propellers, and laser anemometers. In: Dobson, F.; Hasse, L.; Davis, R., eds. Air-sea interaction, instruments and methods. New York: Plenum Press: 11–46.

Businger, J.A. 1986. Evaluating the accuracy with which dry deposition can be measured with current micrometeorological techniques. Journal of Climate & Applied Meteorology. 25: 1100–1124.

Businger, J.A.; Wyngaard, J.C.; Izumi, Y. [and others]. 1971. Flux profile relationship in the atmospheric surface layer. Journal of Atmospheric Science. 28: 181–189.

Carl, D.M.; Tarbell, T.C.; Panofsky, H.A. 1973. Profiles of wind and temperature from towers over homogeneous terrain. Journal of Atmospheric Science. 30: 788–794.

Conklin, P.S.; Knoerr, K.R.; Schneider, T.W. [and others]. 1988. A wind tunnel test of probe shadow effects on a sonic anemometer in two orientations. In: Eighth symposium on turbulence and diffusion. Boston, MA: American Meteorological Society: 108–111.

Dahlquist, G.; Bjorck, A. 1974. Numerical methods. Englewood Cliffs, NJ: Prentice Hall. 573 p.

Delaney, A.C.; Fitzjarrald, D.R.; Lenschow, D.H. [and others]. 1986. Direct measurements of nitrogen oxides and ozone fluxes over grassland. Journal of Atmospheric Chemistry. 4: 429–444.

Dickerson, R.R.; Delany, A.C.; Wartburg, A.F. 1984. Further modification of a commercial NO_x detector for high sensitivity. Review of Scientific Instruments. 55: 1995–1998.

Drummond, J.W.; Voltz, A. 1982. Optimized chemiluminescence detector for tropospheric NO_x measurements. In: 2nd symposium on the composition of the non-urban troposphere. May 25–28. Williamsburg, VA: Cosponsored by American Meteorological Society; American Geophysical Union and National Aeronautics and Space Administration. Published by AMS, Boston, MA: 17–20.

Finkelstein, P.L.; Kaimal, O.C.; Gaynor, J.E. [and others]. 1986. Comparison of wind monitoring systems. Part I: In situ sensors. Journal of Atmospheric and Oceanic Technology. 3: 583–593.

Fitzjarrald, D.R.; Lenschow, D.H. 1983. Mean concentration and flux profiles for chemically reactive species in the atmospheric surface layer. Atmospheric Environment. 17: 2505–2512.

Fontijn, A.; Sabadell, A.J.; Ronco, R.J. 1970. Homogeneous chemiluminescent measurement of nitric oxide with ozone: implications for continuous selective monitoring of gaseous air pollutants. Analytical Chemistry. 42: 575–579.

Gurvich, A.S. 1962. The pulsation spectra of the vertical component of the wind velocity and their relations to the micrometeorological conditions. Izvestiya Atmospheric and Oceanic Physics. 4: 101–136.

Halfpenny, J.C.; Ingraham, R.P., eds. 1984. Long-term ecological research in the United States: a network of research sites 1984. Available from: Forestry Sciences Lab., 3200 Jefferson Way, Corvallis, OR 97331.

Haugen, D.A.; Kaimal, J.C.; Bradley, E.F. 1971. An experimental study of Reynold's stress and heat flux in the atmospheric surface layer. Quarterly Journal of the Royal Meteorological Society. 97: 168–180.

Hicks, B.B. 1972. Propeller anemometers as sensors of atmospheric turbulence. Boundary-Layer Meteorology. 3: 214–228.

Hicks, B.B.; Baldocchi, D.D.; Hosker, R.P., Jr. [and others]. 1985. On the use of monitored air concentrations to infer dry deposition (1985). NOAA Tech. Memo ERL ARL–141 ATDD. Oak Ridge, TN: National Oceanic and Atmospheric Administration. 65 p.

Hicks, B.B.; Wesely, M.L.; Coulter, R.L. [and others]. 1986. An experimental study of sulfur and NO_x fluxes over grassland. Boundary-Layer Meteorology. 34: 103–121.

Högström, U. 1988. Non-dimensional wind and temperature profiles in the atmospheric surface layer: a re-evaluation. Boundary-Layer Meteorology. 42: 55–78.

Højstrup, J. 1981. A simple model for the adjustment of vertical velocity spectra in unstable conditions downstream of an abrupt change in roughness and heat flux. Boundary-Layer Meteorology. 21: 341–356.

Horst, T.J. 1973a. Spectral transfer functions for a three-component sonic anemometer. Journal of Applied Meteorology. 12: 1072–1075.

Horst, T.J. 1973b. Corrections for response errors in a three-component propeller anemometer. Journal of Applied Meteorology. 12: 716–725.

Kaimal, J.C. 1968. The effect of vertical line averaging on the spectra of temperature and heat-flux. Quarterly Journal of the Royal Meteorological Society. 94: 149–155.

Kaimal, J.C. 1975. Sensors and techniques for direct measurement of turbulent fluxes and profiles in the atmospheric surface layer. Atmospheric Technology. 7: 7–14.

Kaimal, J.C.; Wyngaard, J.C.; Haugen, D.A. 1968. Deriving power spectra from a three-component sonic anemometer. Journal of Applied Meteorology. 7: 827–837.

Kaimal, J.C.; Wyngaard, J.C.; Izumi, Y. [and others]. 1972. Spectral characteristics of surface layer turbulence. Quarterly Journal of the Royal Meteorological Society. 98: 563–589.

Knight, D.H. 1972. Leaf area dynamics of the Pawnee Grassland, 1970–1971. International Biophysical Program Technical Report No. 86. 28 p.

Korrell, A.; Panofsky, H.A.; Rossi, R.J. 1982. Wind profiles at the Boulder tower. Boundary-Layer Meteorology. 22: 295–312.

Kristensen, L.; Fitzjarrald, D.R. 1984. The effect of line averaging on scalar flux measurements with a sonic anemometer near the surface. Journal of Atmospheric and Oceanic Technology. 1: 138–146.

Kristensen, L.; Kirkegaard, P. 1987. Digitization noise in power spectra analysis. Journal of Atmospheric and Oceanic Technology. 4: 328–335.

Lauenroth, W.K.; Milchunas, D.G. 1985. The shortgrass steppe. Fort Collins, CO: Range Science Department and Natural Resource Ecology Laboratory, Colorado State University. 109 p.

Lenschow, D.H.; Delaney, A.C. 1987. An analytical formulation for NO_x and NO_2 flux profiles in the atmospheric surface layer. Journal of Atmospheric Chemistry. 5: 301–309.

Lenschow, D.H.; Kristensen, L. 1985. Uncorrelated noise in turbulence measurements. Journal of Atmospheric and Oceanic Technology. 2: 68–81.

Maeda, Y.; Aoki, K.; Munenemori, M. 1980. Chemiluminesence methods for the determination of nitrogen dioxide. Analytical Chemistry. 52: 307–311.

Massman, W.J.; Zeller, K.F. 1988. Rapid method for correcting the non-cosine response errors of the gill propeller anemometer. Journal of Atmospheric and Oceanic Technology.

McMillen, R.T. 1986. A basic program for eddy correlation in non-simple terrain. NOAA Tech. Memo ERL ARL–147 ATDD. Oak Ridge, TN: National Oceanic and Atmospheric Administration. 32 p.

Monson, R.K.; Sackschewsky, M.R.; Williams, G.J.. III. 1986. Field measurements of photosynthesis, water-use efficiency, and growth in Agropyron smithii (C_3) and Bouteloua gracilis (C_4) in the Colorado shortgrass steppe. Oecologia. 68: 400–409.

Moore, C.J. 1986. Frequency response corrections for eddy correlation systems. Boundary-Layer Meteorology. 37: 17–35.

National Acid Precipitation Assessment Program (NAPAP). 1987. Interim assessment: the causes and effects of acidic deposition. Volume 1. Executive Summary. 100 p.

Ohtaki, E. 1985. On the similarity in atmospheric fluctuations of carbon dioxide, water vapor, and temperature over vegetated fields. Boundary-Layer Meteorology. 32: 25–37.

Panofsky, H.A.; Tennekes, H.; Lenschow, D.H. [and others]. 1977. The characteristics of turbulent velocity components in the surface layer under corrective conditions. Boundary-Layer Meteorology. 11: 355–361.

Paulson, C.A. 1970. The mathematical representation of wind and temperature profiles in the unstable atmospheric surface layer. Journal of Applied Meteorology. 9: 857–861.

Peterson, T.C.; Parton, W.J. [n.d.] Behavior of winds: Pawnee Grasslands—1972–75. Available from: Natural Resource Ecology Lab, Colorado State University, Fort Collins, CO 80523. [Unpublished.]

Press, W.H.; Flannery, B.P.; Teukolsky, S.A. [and others]. 1986. Numerical recipes. New York: Cambridge University Press. 818 p.

Rauzi, F.; Dobrenz, A.K. 1970. Seasonal variation of chlorophyll in western wheatgrass and blue grama. Journal of Range Management. 23: 372–373.

Ray, J.D.; Stedman, D.H.; Wendel, G.J. 1986. Fast chemiluminescent method for measurement of ambient ozone. Analytical Chemistry. 58: 598–600.

Redford, T.G., Jr.; Verma, S.B.; Rosenberg, N.J. 1980. Humidity fluctuations over a vegetated surface measured with a Lyman-Alpha hygrometer and a fine-wire thermocouple psychrometer. Journal of Applied Meteorology. 19: 860–867.

Sehmel, G.A. 1980. Particle and gas dry deposition: a review. Atmospheric Environment. 14: 983–1011.

Sehmel, G.A. 1984. Deposition and resuspension. In: U.S. Dept. of Energy: Atmospheric science and power production. 533–583. Chapter 12. National Technical Information Service. Springfield, VA.

Silverman, B.A. 1968. The effect of spatial averaging on spectrum estimation. Journal of Applied Meteorology. 7: 168–172.

Slemr, F.; Seiler, W. 1984. Field measurements of NO_x and NO_2 emissions from fertilized and unfertilized soils. Journal of Atmospheric Chemistry. 2: 1–24.

Smith, S.D.; Anderson, R.J. 1984. Spectra of humidity, temperature, and wind over the sea at Sable Island, Nova Scotia. Journal of Geophysical Research. 89: 2029–2040.

Steffenson, D.M.; Stedman, D.H. 1974. Optimization of the operating parameters of chemiluminescent nitric oxide detectors. Analytical Chemistry. 46: 1074–1709.

Webb, E.K.; Pearman, G.I.; Leunig, R. 1980. Correction of flux measurements for density effects due to heat and vapor transfer. Quarterly Journal of the Royal Meteorological Society. 106: 85–100.

Wendel, G.J.; Stedman, D.H.; Cantrell, C.A. [and others]. 1983. Luminol-based nitrogen dioxide detector. Analytical Chemistry. 55: 937–940.

Wesely, M.L.; Eastman, J.A.; Cook, D.R. [and others]. 1978. Daytime variations of ozone eddy fluxes to maize. Boundary-Layer Meteorology. 15: 361–373.

Wesely, M.L.; Eastman, J.A.; Stedman, D.H.; [and others]. 1982. An eddy-correlation measurement of NO_2 flux to vegetation and comparison to O_3 flux. Atmospheric Environment. 16: 815–820.

Wesely, M.L.; Hicks, B.B. 1977. Some factors that affect the deposition rates of sulfur dioxide and similar gases on vegetation. Journal of the American Pollution Control Association. 27: 1110–1116.

Wetstone, Gregory. 1980. Air pollution control laws in North America. Environmental Law Reporter, The Problem of Acid Rain and Snow. 10: 50,000–50,020.

Williams, E.J.; Parrish, D.D.; Fehsenfeld, F.C. 1987. Determination of nitrogen oxide emissions from soils: results from a grassland site in Colorado, United States. Journal of Geophysical Research. 92: 2173–2179.

Wyngaard, J.C. 1971. Spatial resolution of a resistance wire temperature sensor. Physics of Fluids. 14: 2052–2054.

Wyngaard, J.C. 1988. Flow distortion effects on scalar flux measurements in the surface layer: implications for sensor design. Boundary-Layer Meteorology. 42: 19–26.

Wyngaard, J.C.; Cote', O.R.; Izumi, Y. 1971. Local free convection, similarity, and the budgets of shear stress and heat flux. Journal of Atmospheric Science. 28: 1171–1182.

APPENDIX A. Description of Fast Response Chemical Sensors[1]

An earlier version of this research project was designed to measure the dry deposition of NO_2, NO_x (principally $NO + NO_2 +$ peroxyacetyl nitrate [PAN]), ozone, and SO_x to grassland during winter and summer months. However, the SO_x sensor was not available during the field season because it was still undergoing further development in the laboratory to improve sensitivity and response time. This chemical analysis project included the installation, operation, and maintenance of the intake system, detectors, and the zero and calibration system.

The instruments were housed in the shelter, and air was brought from the tower to the shelter using a high-volume sample pump. The arrangement avoided introducing extraneous turbulence to the mean wind flow and kept the instruments in a temperature-controlled environment. The intake system consisted of a 26.5-m-long, 5/8-inch-i.d. Teflon tube through which air was drawn at ca. 160 l/min using a high-volume air pump (Fuji ring compressor). The flow rate decreased with time (table A1). The chemical sensors sampled from the main air stream and returned their exhaust downstream of the sampling manifold to keep the pressure drop across the instruments to a minimum. The interference caused by adsorption/desorption was minimized by using large-bore Teflon tubing. Although the length of sample tube slowed the response of the chemical instruments and cut off some of the high-frequency flux data, the need for a complex temperature correction was eliminated by housing the instruments in a temperature-controlled shelter. Table A2 presents a summary of the chemical instruments and their specifications.

Chemiluminescent Ambient Air Monitors (CAAM)

The same instrument design was adapted to measure nitrogen dioxide (Wendel et al. 1983) and ozone (Ray et al. 1986) by changing the fluorescent reagent used. The sample flowed through a detection cell and over a filter pad wetted with the fluorescent reagent (see fig. A1). A blue-sensitive photomultiplier tube (PMT) monitored the light produced. The fluid and air exited at the bottom of the reaction cell and were separated by gravity in the catch reservoir. The fluid flow rate was 1 ml/min and the air flow rate was 10 l/min. The response of these instruments was pressure-dependent.

For the detection of nitrogen dioxide a basic solution of luminol (5-amino-2,3-dihydro-1,4-phthalazinedione) was used (Maeda et al. 1980). The solution was comprised of 0.05 M NaOH, 0.1 M Na_2SO_3, 2 x 10^{-4} M luminol, and 0.05% vol/vol t-butanol. The solution was
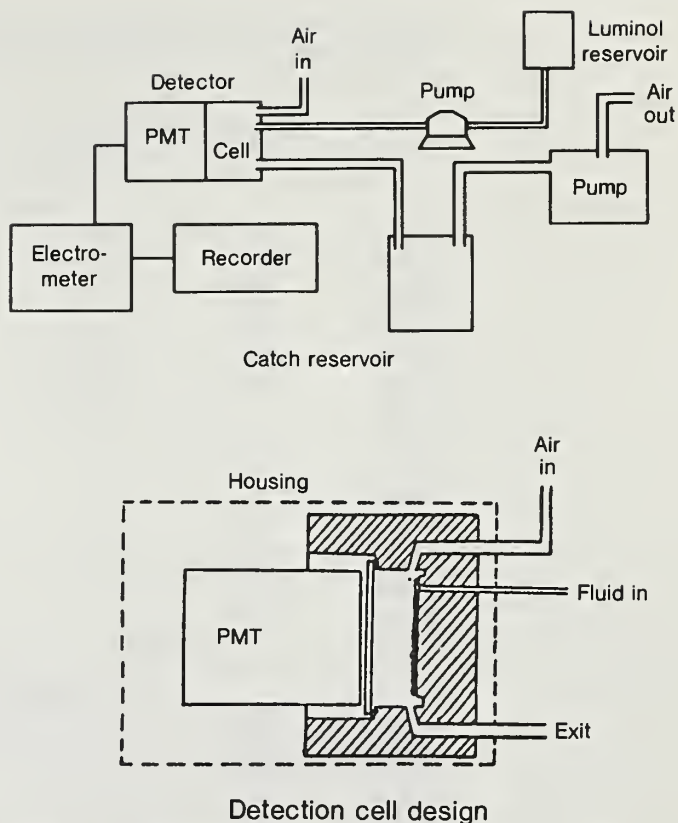
Figure A1.—Schematic diagram of the Chemiluminescent Ambient Air Monitor, with an enlargement of the detection cell, which is machined from black Delrin; a glass window seals the cell.

used once and then discarded. Operating under these conditions, the sensitivity was ca. 0.2 μA/ppb (parts per billion volumetric mixing ratio) and the response was linear from 0.1 ppb (fig. A2). The response of the instrument did decay with time after a fresh solution was installed and the filter pad in the detection cell changed, probably because of degradation of the filter pad and aging of the solution. The solution was replaced approximately weekly and the instrument recalibrated (table A1 gives details of the calibration changes). When operated in the laboratory the instrument responded to a square wave pulse of NO_2 introduced to the intake of the instrument within 0.2 seconds. Under field conditions, the response to a square wave pulse of clean air introduced to the system at the tower was slower (0.7 s) because broadening of the sample occurred in the intake system (fig. A3). The detection limit was 0.14 ppb.

For the analysis of ozone the basic luminol solution was exchanged for a solution of eosine-Y in ethylene glycol. The dye solution was recycled after each batch had passed through the instrument. The ozone detector was calibrated by comparing the output signal with that from a slow-response UV photometric ozone monitor (TECO model 49A). The sensitivity was 0.12 μA/ppb and the detection limit was <1 ppb in the field. In the laboratory the response of the instrument was 7 Hz, which decreased under field conditions to 1.4 Hz because of the broadening that occurred when sampling through the long intake tube (fig. A4).

17

Table A1.—Dates of calibration and field notes for the chemical sensors operated at the Pawnee Grasslands field site (Dec. 1, 1986, through Feb. 2, 1987, and May 1, 1987, through July 27, 1987).

Date	Julian date	Flow rate[a] (L/min)	Ozone[b,c] (ppb/V)	$NO_2{}^c$ (ppb/V)	$NO_x{}^d$ (ppb/V)
Winter experiment					
11–Dec	345	178	Fresh	11.1[e]	3.13
17–Dec	351			3.2	2.78[f]
19–Dec	353		15:55		
22–Dec	356			2.53, 3.92[e]	
24–Dec	358		13:10		
29–Dec	363		Recycled		
31–Dec	365			e,g	
2–Jan	2		11:45		
7–Jan	7		Recycled		
8–Jan	8		h	2.13, 21.3[i]	2.77
12–Jan	12		Recycled		
16–Jan	16		Recycled		
20–Jan	20		Recycled	29.4	3.27
21–Jan	21			e	
24–Jan	24			e	
27–Jan	27		k	44.7	3.21
29–Jan	29		Recycled		
2–Feb	33	End of winter experiment.			
Summer experiment					
13–May	133		Fresh	e	1
14–May	134	159		10.0	0.038
18–May	138		11:45	15.7[m], 12.1[e]	0.034
21–May	141		12:30	3.13[e,h,n,o]	0.034[p]
22–May	142			o	
23–May	143			2.1[e,n]	
24–May	144		refill (am)		
26–May	146			1.079[e,n,o,q]	
27–May	147			3.92	0.04
29–May	149		12:25		
1–Jun	152	158	r	7.41	
2–Jun	153		r		
5–Jun	156		9:05	1.56[e,m,n]	
8–Jun	159			s	t
9–Jun	160				u
10–Jun	161			4.39[e]	
11–Jun	162		8:46		
15–Jun	166		11:00		
16–Jun	167			7:83	0.083[p]
18–Jun	169		k	7.98	0.039
22–Jun	173		7:48		
23–Jun	174	158[v]		h,k	
24–Jun	175	164			
30–Jun	181	162	6:40[w]	8.98	0.048[p,x]
2–Jul	183			6.14	0.029
4–Jul	185			y	
6–Jul	187		7:48		0.031[p]
7–Jul	188			3.67[e,k]	
10–Jul	191			17.7, 2.71[h]	0.051
13–Jul	194		6:47		
15–Jul	196	z		6.33	0.038
16–Jul	197	aa			
20–Jul	201		11:30		
27–Jul	208	Site shutdown			

[a]Measured using a dry gas meter attached to the exhaust of the large sample pump, correcting for the flow through the NO_x analyzer that is not returned to the sample inlet.

[b]Wherever possible, the times when the dye solution was recycled is reported.

[c]The calibration factor is in units of ppb/V, the calibrated sensitivity in parts per billion mixing ratio per volt observed by the data acquisition system when the instrument is working with a full-scale deflection of 10 μA.

[d]10 nA full-scale deflection.

[e]Fresh solution.

[f]Converter heater repaired.

[g]Solution changed, but neither old nor new solutions calibrated.

[h]Changed target pad.
[i]Changed full-scale deflection to 100 µA.
[j]Changed zero air traps.
[k]Air pump replaced.
[l]Response of NO$_x$ analyzer has changed by a factor of 100, which implies an electronic rather than a chemical fault is to blame. The response of the NO$_x$ analyzer is also very noisy.
[m]Luminol flow stopped.
[n]No calibration of old solution.
[o]No luminol left.
[p]Oxygen tank empty.
[q]High calibration, signal may not have stabilized.
[r]TECO photometric ozone monitor recalibrated.
[s]No calibration possible as NO$_x$ analyzer off line.
[t]Plugged frit in ozone line.
[u]Repair of ozone generator in Denver University laboratories.
[v]Change air filters in main sample line, system is off-line.
[w]Reservoir dry before refill.
[x]Plugged sample intake.
[y]Broken air pump.
[z]Zero air system self destructs, trap explodes.
[aa]Replace zero air trap.

Table A2.—Summary of the characteristics of the chemical sensors used during the field study.

| Chemical measured	Instrument name	Sensitivity	Comments
Total NO$_x$	NO$_x$ box	0.3 µA/ppb	Requires high-pressure O$_2$ cylinders for O$_3$ production; large vacuum pumps; cooled red-sensitive PMT; high power (240 v). Fast response <1 sec NO$_x$ by catalytic reduction using Mo turnings at 400 °C. Stable calibration.
NO$_2$	CAAM 2	0.2 µA/ppb	Uses a basic luminol solution which cannot be recycled. Each batch of reagent requires calibration. Sensitivity of solution decreases with time. Calibrate and check target pad weekly. Response time <1 sec. Portable low power required.
Ozone	Teco 49A	0.2 mv/ppb	EPA standard. Slow response.
Ozone	CAAM 1	0.12 µA/ppb	Uses eosine-Y in ethylene glycol which can be recycled but some sensitivity is lost with use. Response time <1 sec. Calibrate using UV photometric instrument. Period of unattended use limited by reservoir size. Target pad checked weekly. Portable low power required.
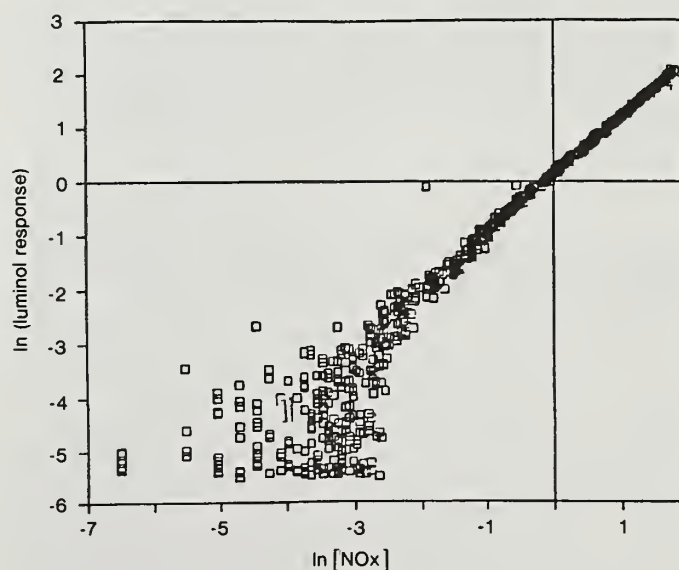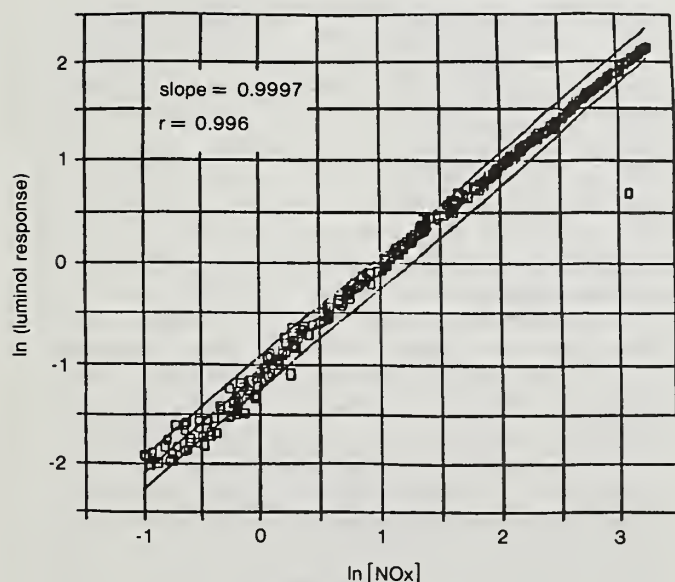
Figure A2.—The response of the total nitrogen oxides detector and the nitrogen dioxide detector to low concentrations of nitrogen dioxide.
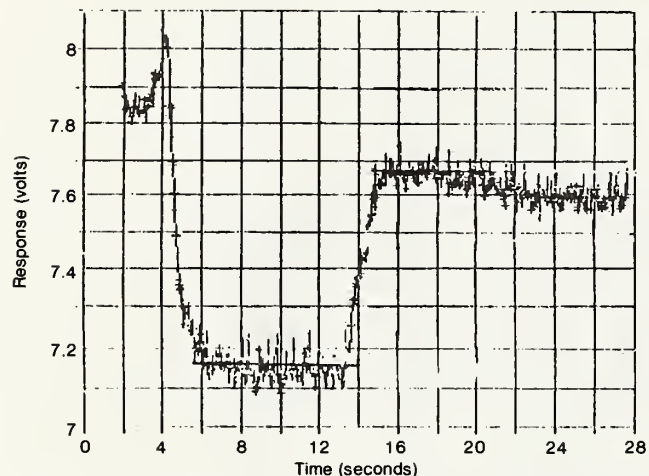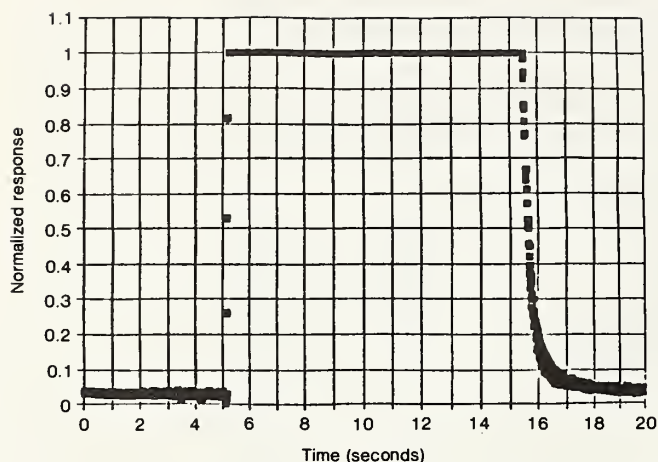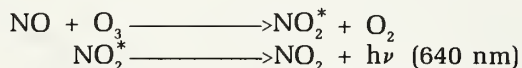
19

Figure A3.—Frequency response of the nitrogen dioxide detector: (a) to a square wave pulse of nitrogen dioxide in the laboratory and (b) to a square wave pulse of zero air introduced to the tower inlet in the field.
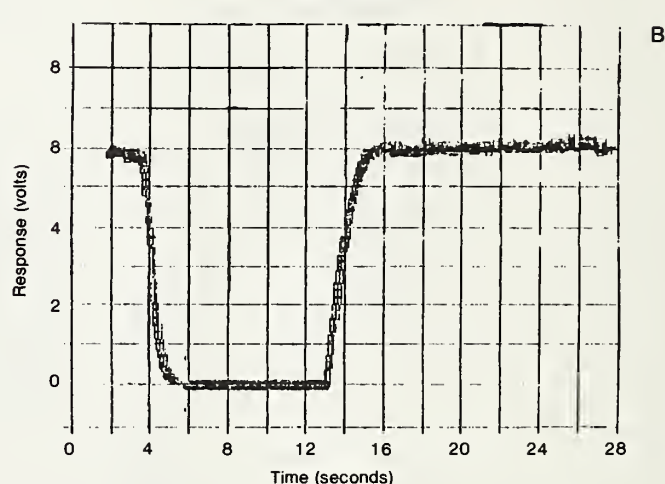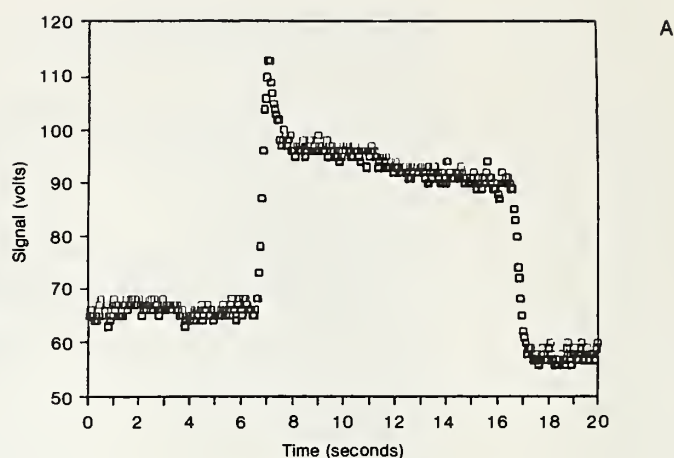
Figure A4.—Frequency response of the ozone detector: (a) to a square wave pulse of ozone in the laboratory and (b) to a square wave pulse of zero air introduced to the tower inlet in the field.

Total NO_x Analyzer

NO reacts with ozone forming electronically excited nitrogen dioxide. At reduced pressure the excited nitrogen dioxide decays to the ground state, emitting a photon:

$$NO + O_3 \longrightarrow NO_2^* + O_2$$
$$NO_2^* \longrightarrow NO_2 + h\nu \quad (640 \text{ nm})$$

The intensity of light produced is proportional to the concentration of NO, forming the basis for the total NO_x analyzer (Fontijn 1970).

The higher oxides of nitrogen were reduced to NO by passing the sample gas through a hot molybdenum converter at 400°C. The principle species reduced were NO_2 and PAN (Dickerson et al. 1984). Nitric acid is known to pass through the length of the sample tubes to reach the converter housed in the shelter, but it has been shown in the past to have a response time larger than 120 s. This slow response is presumed to arise from a "chromatographic" effect of HNO_3 sticking and releasing from the intake tubing. The response time for nitric acid is too slow to allow correlation with changes in vertical wind velocities to determine HNO_3 fluxes.

The reduced sample gas was mixed with excess ozone prior to entering the reaction chamber in front of a cooled red-sensitive photomultiplier tube (EMMI 9658). The walls of the reaction chamber were gold-plated to enhance reflectivity and provide an inert surface. Ozone was produced by passing 250 ml/min of O_2 through three parallel discharge tubes; a water bubbler in the ozone line decreases the background signal (Drummond and Voltz 1982). The analyzer is shown schematically in figure A5. The photomultiplier tube output was fed to a programmable electrometer (Keithley 18000–20).

The instrument was operated with a chamber vacuum of 5–10 torr and a sample flow rate of approximately 4 l/min. Under these conditions the instrument response was ca. 0.3 nA/ppb with background noise equivalent to a detection limit of ca. 0.07–0.2 ppb; however, at times the noise was greater than this. The sensitivity of the instrument was constant throughout each experimental period, as shown in table A1. The change in sensitivity between the two experimental periods was due to a fault in the electrometer. The instrument was less sensitive when ambient air was used for ozone generation, which was necessary when the oxygen cylinder had emptied. The response of the analyzer to NO_2 was linear until

20

the signal to noise ratio approached unit (fig. A2). When operated in the laboratory, the instrument responded to a square wave pulse of 10 ppb of NO within 0.3 s (fig. A6). However, when operated in the field and sampling through the long intake tube, the instrument responsed somewhat more slowly at 0.9 s.

Experiments carried out by heating the intake gases to the analyzer while keeping the concentration of span gas constant showed no deviation in response; therefore, the response of the instrument was not pressure-dependent. This is consistent with the conclusions of Steffenson and Stedman (1974) provided constant-volume vacuum pumps are used.

Zero and Calibration Systems

The instruments used in this study are highly sensitive and consequently are susceptible to some baseline drift;
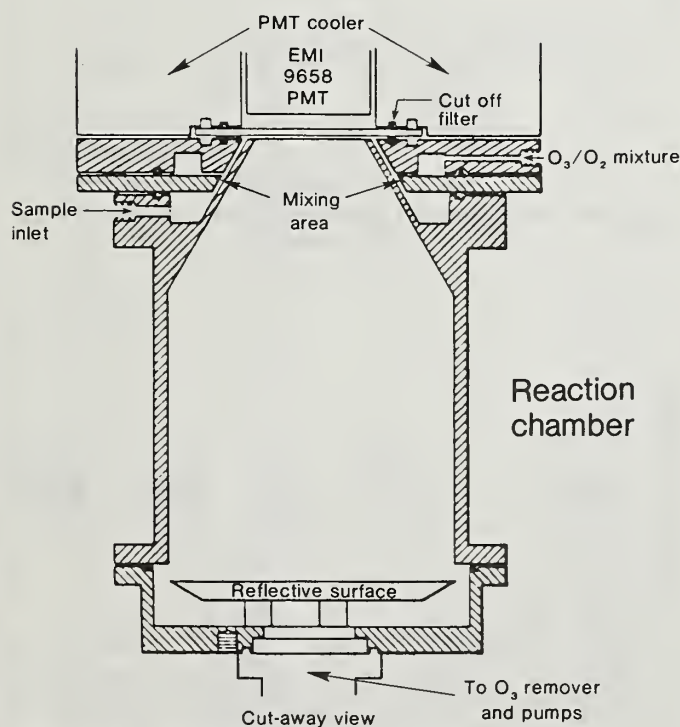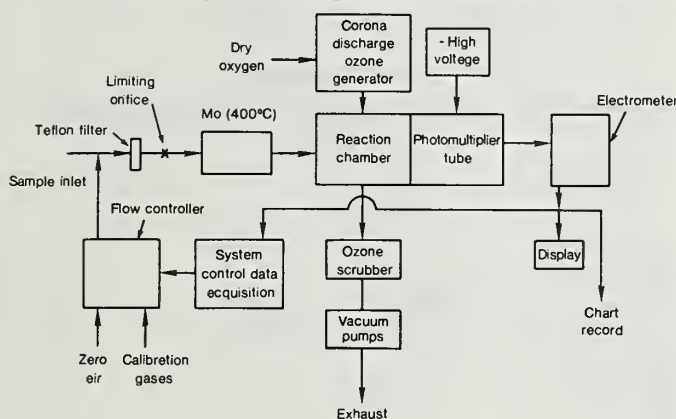

Figure A5.—Schematic diagram of the total oxides of nitrogen detector with a sectional view of the reaction chamber.
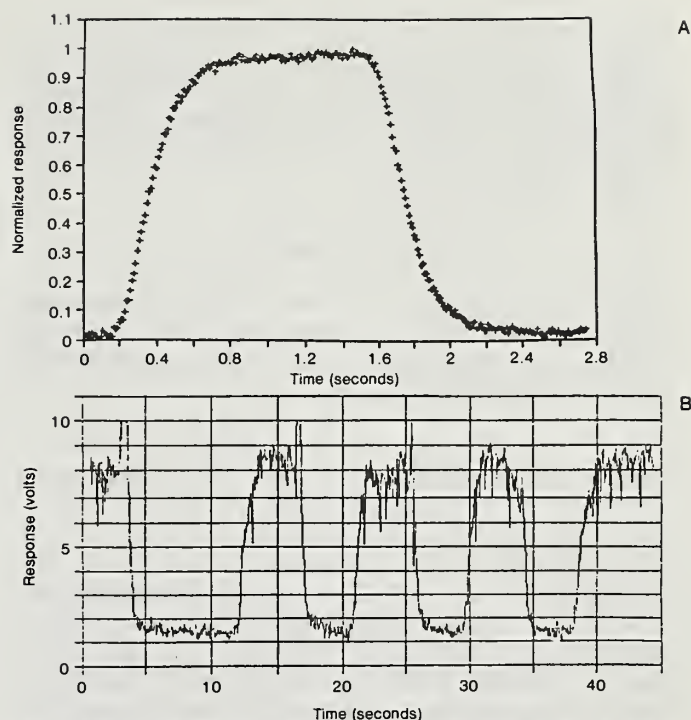

Figure A6.—Frequency response of the total NO_x analyzer: (a) to a square wave pulse of 10 ppb NO in the laboratory and (b) to a square wave pulse of zero air introduced to the tower inlet in the field.

thus, it is necessary to keep track of the response of these instruments to clean, unpolluted air.

"Zero air" was prepared by scrubbing ambient air using a series of traps. The first contained ferrous sulphate which reduced NO_2 to NO which was then removed by a second trap filled with Purafil. A third trap filled with activated charcoal removed ozone. A compressor was used to fill a 30-gallon tank to a pressure of 100 psi with zero air. At the end of each sampling period zero air was introduced at the inlet to the main sample line through 3/8-inch-i.d. black Teflon tubing. The flow of air to the tower intake, ca. 170 l/m, was sufficient to overvent the main sample flow at a constant flow rate for approximately 3 minutes.

The system was calibrated on a weekly basis. This was achieved by adding a known flow of span gas to the zero air supply while the zero air flow rate was still constant. The NO_x analyzer was calibrated using a span gas mixture of 10 ppm NO in N_2. The NO_2 CAAM instrument was calibrated using a 1000 ppm NO_2 in N_2 standard; the concentration of NO_2 reaching the instruments was checked against the NO_x analyzer.

Future Work

As soon as the SO_x analyzer is functioning in a reliable and predictable mode, field measurements of the flux of SO_x to prairie grassland and snow should be performed. Other chemical measurements of interest include the measurement of the flux of NO_y (NO_x + HNO_3) using a new intake system (currently under development) for the chemiluminescent NO_x analyzer used in this study. The NO_x analyzer in its present configuration is capable

of measuring the flux of NO, this along with the concentration of PAN should be measured to determine a nitrogen flux budget. The concentration of PAN should be determined using a chromatographic technique developed in these laboratories based on a luminol detector (Burkhardt et al. 1987).

Acknowledgments

APPENDIX B. Eddy Correlation System Response Characteristics

This appendix outlines the method we used to correct the flux measurements for sensor inadequacies such as slow response characteristics, spatial averaging effects, and sensor mismatching. The method is similar to Moore's (1986) in that it uses the frequency-dependent instrument response functions and the spectral and cospectral distribution functions associated with atmospheric turbulent variances and fluxes to derive the correction factors. It differs from Moore's (1986) method in that it employs chemical sensors, treats aliasing differently, and includes the effects of mismatched sensors.

Specifically, the correction, ΔF, of the true flux, F, of a quantity with specific density, q, is estimated as follows:

$$\frac{\Delta F}{F} \equiv 1 - \frac{\int_o^\infty H_{wq}(n)C_{wq}(n)dn}{\int_o^\infty C_{wq}(n)dn} \qquad [B1]$$

where the true flux $F = \int_o^\infty C_{wq}(n)dn$, $\Delta F/F$ represents the percentage flux loss, and $H_{wq}(n)$ is the total system cospectral response function associated with the sensors for the vertical wind velocity, w, and the quantity, q. $H_{wq}(n)$ is the product of the separate response functions associated with the data logging system, sensor frequency response, sensor size, sensor separation, and sensor mismatch, and $C_{wq}(n)$ is the atmospheric cospectrum of w and q as a function of frequency, n.

The response functions appropriate to each of the various instruments and the data logging system are described.

Fast Response Chemical Sensors (O_3, NO_2, NO_x)

At present the fast response chemical sensors are housed in an air-conditioned shelter about 26.5 m south of the meteorological tower. The sampled air is brought rapidly into the shelter through a long Teflon tube, whose intake is positioned on the tower near the anemometers and temperature sensor. The response times of the sensors were determined in situ by a series of concentration step changes that involved alternately switching between passing ambient air and passing clean air (zero

concentration) through the intake tube and into the sensors.

Figures B1–B3 give examples of the data gathered during one of the response time tests and table B1 gives the results of the tests. The tests were performed on three
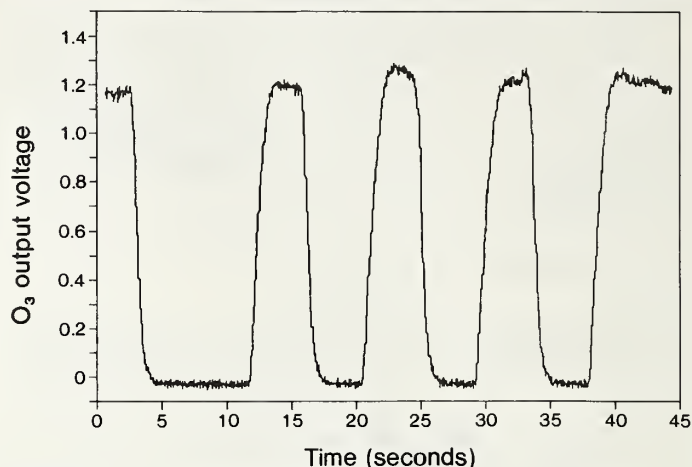

Figure B1.—Response time tests for fast response ozone sensor, June 24, 1987.
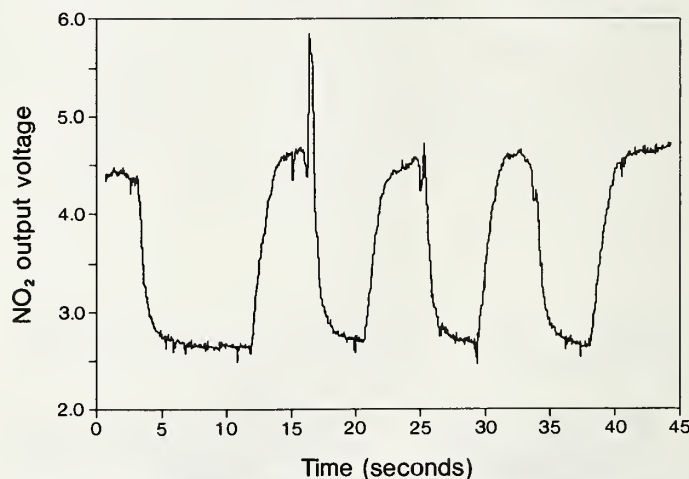

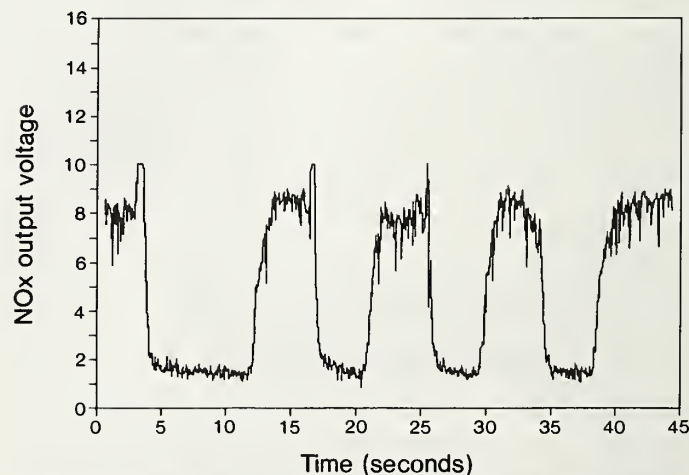Figure B2.—Response time tests for fast response NO_2 sensor, July 24, 1987.

Figure B3.—Response time tests for fast response NO_x sensor, July 24, 1987.

separate occasions and usually consisted of three or four positive and negative step changes. For a negative step change (decreasing from ambient to zero concentration), the data were fit with a decreasing exponential, $e^{-t/\tau-}$, and the best response time, $\tau-$, was found using a least squares minimization technique. (Here t represents time.) For a positive step change (increasing from zero to ambient concentration), the same method was employed except that the exponential, $e^{-t/\tau+}$, was replaced by $(1 - e^{-t/\tau+})$. Finally, only data between 20% and 80% of maximum were used to fit the curves. The ozone sensor (fig. B1), which usually provides the least noisy signal, has a response time of about 0.7 s. Although its response time was independent of the magnitude of the step change, the ozone sensor does display some slight asymmetry in response to positive and negative step changes with the response time $\tau-$ being slightly shorter than $\tau+$. This asymmetry is also observed in the laboratory and is thought to be related to adsorption and desorption of ozone by the intake tube walls. The response time of 0.7 s is also slower (by a factor of about 2) than that observed in the laboratory (Ray et al. 1986 and appendix A). Again, this is consistent with the adsorption and desorption processes, which will tend to lengthen the response time by adding ozone to the air stream as the concentration decreases to zero and by removing ozone from the air stream as the concentration increases to ambient. In addition, the mixing of gas samples and the resulting smearing of the high frequency changes in gas concentrations by the highly turbulent flows inside the Teflon

tube (Reynolds number about 10^4) may also contribute to this lengthening of the response time of the chemical sensors over what has been observed in the laboratory.

The response times of the NO_2 and NO_x sensors (figs. B2 and B3, respectively) were more difficult to obtain because the sensors are noisier than the ozone sensor. For the NO_2 sensor the response time is 0.7 s and it is 0.9 s for the NO_x sensor. These response times were found by the same method as the ozone sensor except that there were fewer useful data sets with which to do the curve fitting. In the case of the NO_x sensor, a low pass RC analog filter with a 0.04-s time constant had to be incorporated to remove the high frequency noise in the signal. These two sensors, as does the ozone sensor, also display a slight asymmetry in their response to positive and negative step changes, and a longer response time than observed in the laboratory (Wendel et al. 1983, Wesely et al. 1982). Again, as with ozone, adsorption and desorption of these gases by the tube walls and the turbulent flows inside the tube are thought to be largely responsible for these differences. These last two figures also show another problem peculiar to these two sensors. In both cases, the NO_2 and NO_x concentrations increase above ambient just prior to the region where the concentrations begin to decrease to zero. The cause for this pulse of gas is unknown, but it may be related to the valves that switch the clean air flow and the ambient air flow. For the response time tests this problem was not a consideration.

It is important to note that, in addition to the response times, these response time tests also give the lag or delay time required to move the air from the mouth of the intake tube to the sensors. The delay time is represented on figures B1–B3 as the time from input of clean air at the mouth of the intake tube (t≈0) to the time at which the concentration begins to decrease. These results show that the lag time was 2.0 s at a flow rate of 155 l/min. This direct method of determining the delay time was also independently verified from measurements of the flow rate and the length and cross-sectional area of the intake tube (inside diameter of intake tube = 5/8 inch). This independent estimate of the delay time was 2.1 s. For computing eddy correlation fluxes, the analog signals from these chemical sensors are shifted digitally in time by 2 s.

Finally, these response time tests also show that the zero concentration of these gases do not necessarily correspond to a zero voltage reading of the instruments. This bias in the data signal was intentional and was included in data calibration and reduction. Further details on the calibration of these chemical sensors is discussed in appendix A.

With these response times, the response function that describes the dynamic frequency response of these chemical sensors is given as follows:

$$T_d(n) = 1/[1 + (2\pi n\tau)^2]^{1/2} \qquad [B2]$$

Here we assume that these sensors are "first order systems" (Brock and Nicolaidis 1985).

Table B1.—Optimal response times of fast response chemical sensors.[a]

Test date	Sensor response time (seconds)		
	O_3 (CAAM1)	NO_2 (CAAM2)	NO_x
January 28, 1987			
$\tau-$	0.65	--	--
$\tau-$	0.66	--	--
$\tau-$	0.60	--	--
$\tau+$	1.02	--	--
$\tau+$	0.94	--	--
$\tau+$	1.07	--	--
June 3, 1987			
$\tau-$	0.62	0.72	--
$\tau-$	0.63	0.63	--
$\tau-$	0.64	0.48	--
$\tau+$	0.79	--	--
$\tau+$	0.83	--	--
$\tau+$	0.71	--	--
June 24, 1987			
$\tau-$	0.58	--	--
$\tau-$	0.66	--	--
$\tau-$	0.67	--	--
$\tau-$	0.56	--	0.95
$\tau+$	0.76	0.79	0.93
$\tau+$	0.87	0.63	0.84
$\tau+$	0.83	0.73	0.84
$\tau+$	0.84	0.65	0.79

[a]$\tau-$ equals response time to step change from ambient to clear air and $\tau+$ equals response time to step change from clean air to ambient.

In addition to the dynamic frequency response, another important question that needs to be addressed is that of spatial averaging effects caused by sampling a volume of air as it is drawn through the intake tube into the reaction chambers. This effect, which is likely to be important whenever the sampled volume of air is large and the sensor response is sufficiently fast, results from the fact that a measurement of concentration is not made at a point, but rather the measurements of concentration represent the average concentration within a finite volume of air that has been drawn into the sensor. These spatial averaging effects (in the form of line averaging rather than volume averaging) have been investigated for sonic anemometers (Silverman 1968, Kaimal et al. 1968, Horst 1973a), and for platinum wire thermometers (Kaimal 1968, Wyngaard 1971). They have also been investigated for the Lyman-Alpha Hygrometer by Andreas (1981) in the form of volume averaging over a right circular cylinder.

For our measurement system the response function associated with volume averaging (assuming a spherical volume) is given by the following equation, which is derived in appendix C.

$$T_v(n) = \frac{10}{3\pi(k_1R)^2} \int_0^\infty\int \frac{T_*(k_1R,x_2,x_3)}{(1+x_2^2+x_3^2)^{11/6}} \, dx_2 \, dx_3 \qquad [B3]$$

where R is the radius of the sphere over which we are averaging and k_1 is the wave number in the direction of the mean horizontal wind and by Taylor's hypothesis, $k_1 = 2\pi n/\bar{u}$, where $\bar{u}$ is the mean horizontal wind speed. Here $T_*(k_1R,x_2,x_3)$ is defined as:

$$T_*(k_1R,x_2,x_3) = \frac{9}{4x_3^2}\left[\int_0^{\pi/2} \sin2\theta \, \sin(k_1Rx_3\cos\theta) \atop J_0(k_1R\,(1+x_2^2)^{1/2} \, \sin\theta) \, d\theta\right]^2 \qquad [B4]$$

where J_0 is a Bessel function. Equations [B3] and [B4] were integrated numerically (see appendix C and discussion below), and the results are given in figure B4, which is a plot of $T_v(k_1R)$. This figure and equation [B1] show that spatial averaging effects are important only when $T_v(k_1R)$ departs significantly from a value of unity,
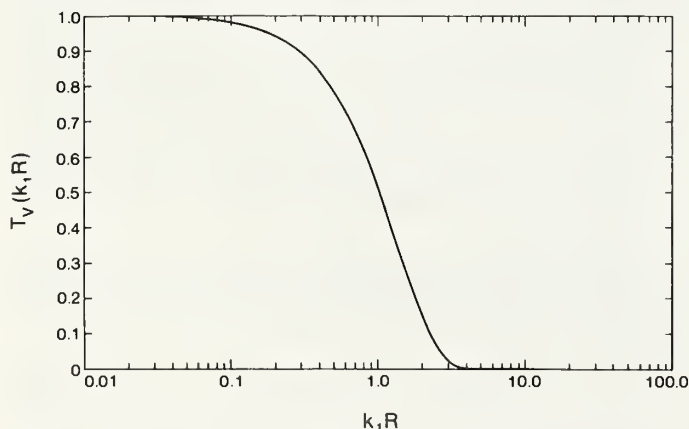

Figure B4.—Spectral transfer function, $T_v(k_1R)$, associated with spherical volume averaging of the O_3, NO_2, and NO_x concentration fluctuation measurements. $k_1 = 2\pi n/\bar{u}$.

which occurs whenever $k_1R \gtrsim 1$ or, equivalently, whenever the physical dimensions of a turbulent atmospheric eddy are comparable to or smaller than the radius of the averaging volume. Because T_v is, in general, a function of wind speed, the importance of the volume averaging effects can only be assessed by evaluating the flux loss, equation [B1], as a function of wind speed with and without $T_v(n)$ as a component of $H_{wq}(n)$. This will be discussed below. It should also be noted that the spherical volume over which we are averaging becomes distorted by the wind speed; however, Taylor's hypothesis allows for this and thus k_1 becomes a function of the mean wind speed.

Finally, an estimate of the radius, R, is needed. A typical value of R can be estimated from measurements of the intake flow rate, Q, and the sampling frequency, n_s, as follows: $R = [3Q/(4\pi n_s)]^{1/3}$. This basically assumes that for any given period of time, Δt, the volume $Q\Delta t$ is divided into $n_s\Delta t$ spherical subvolumes for each of which we make a concentration measurement. Given typical flow rates of about 150–170 l/min and a sampling rate of 10–20 Hz, 4 cm is a reasonable estimate for the radius R. This value will be used in the next section for calculating flux loss estimates.

Gill UVW Anemometers

Like the chemical sensors, the 3-axis Gill propeller anemometer is also a first order system; hence, the response function associated with this instrument is also described by equation [B2]. However, the response time, τ, associated with the Gill propeller is not a constant as it is with the chemical sensors; rather, it is dependent largely upon the horizontal wind speed, u, and is given by $\tau = D/u$. The response length, D, has been determined from wind tunnel experiments to be a function of the attack angle of the wind. For a propeller measuring the horizontal wind speed, however, this effect is small, and D can be considered constant and equal to 1 m. For the vertical propeller, on the other hand, D is not necessarily constant but will increase from about 1 m to 2 m as the flow deviates from axial to about 80° off axis and will continue to increase to infinity at 90° off axis. Therefore, in general the response time of the Gill propellers varies constantly with the flow velocity. For the purposes of this work, the response time of the horizontal propellers is assumed to be 1 m/$\bar{u}$ and that of the vertical propeller 2.5 m/$\bar{u}$. Therefore, the response function for Gill propellers, which uses these latter two response times, is an approximation to the true response function. For more details on the subject of response characteristics of these sensors, see Hicks (1972) and Busch et al. (1980).

Sensor Mismatching

In addition to the errors in flux measurements caused by slow response times of individual sensors, mismatching of sensors used for flux measurements can introduce

further errors. Mismatching errors are produced whenever sensors have different response characteristics. When this occurs, there is a relative phase shift in the time series gathered by the different sensors. If the relative phase shift is small, then the loss of correlation (or flux) between the two time series is also small. However, as the relative phase shift increases, the two time series can become increasingly uncorrelated and, hence, the flux measurements may be seriously underestimated. In general, all sensors are somewhat mismatched unless they happen to have exactly the same response characteristics and, therefore, exactly the same response functions. However, mismatching is most serious when flux measurements are made with two first order sensors that have very different response times or when a slow response sensor is used in conjunction with a fast response sensor. In our case this corresponds to (1) the chemical flux measurements made using a Gill propeller during low or high wind speeds or at all wind speeds using a sonic anemometer and (2) the heat flux measurements made with the relatively slow responding vertical Gill propeller and the much faster responding temperature sensor.

The transfer function associated with mismatching is given simply as $T_m(n) = \cos(\varphi_1 - \varphi_2)$, where φ_1 and φ_2 are the phase shifts introduced into the measurements by sensor number 1 and number 2, respectively. For first order systems, the phase shift $\varphi = \tan^{-1}(2\pi n\tau)$, from which it follows that $\cos\varphi = 1/(1 + (2\pi n\tau)^2)^{1/2}$ and $\sin\varphi = (2\pi n\tau)/(1 + (2\pi n\tau)^2)^{1/2}$. Therefore, using these latter two relations and the definition of $T_m(n)$ it is straightforward to show that:

$$T_m(n) = \frac{1 + (2\pi n)^2 \tau_1 \tau_2}{[(1 + (2\pi n\tau_1)^2)(1 + (2\pi n\tau_2)^2)]^{1/2}} \quad [B5]$$

Again, this transfer function is appropriate to first order systems and is most significant whenever τ_1 is very different from τ_2.

Using the slower responding chemical sensors and the faster responding vertical sonic anemometer can also introduce mismatching errors in the O_3, NO_2, and NO_x flux measurements. For this case, we assume that [B5] is valid but that the response time for the sonic (e.g., τ_1) is zero, so the formulation of $T_m(n)$ simply reduces to $1/(1 + (2\pi n\tau)^2)^{1/2}$, where τ is the response time of the chemical sensors. This approximation will produce a slight overestimation of the flux loss because the sonic anemometer does, in fact, produce a small phase shift in the spectra at higher wave numbers.

Sonic Anemometers

Unlike the chemical sensors or the Gill propellers, the sonic anemometer is not limited by a slow response time. Rather, its limitations are associated with line averaging effects (which is the one-dimensional equivalent to the volume averaging effects of the chemical sensors discussed earlier). The response function associated with line averaging of the vertical velocity is taken from

Kaimal et al. (1968) and is given in the following equation:

$$T_{l_w}(n) = \frac{2\Gamma(4/3)}{\Gamma(1/2)\,\Gamma(5/6)\,(k_1 l_w)^2} \int_o^\infty \left[\frac{\sin^2(k_1 l_w x_3/2)}{(x_3/2)^2} \right] x$$

$$\left[\frac{1}{(1 + x_3^2)^{7/3}} + \frac{3/8}{(1 + x_3^2)^{4/3}} \right] dx_3 \quad [B6]$$

where l_w is the vertical sonic path (= 25 cm for our sonic), Γ is the Gamma function, and $k_1 = 2\pi n/\bar{u}$ as was discussed above. The expression given in [B6] has been adapted from Kaimal et al. (1968) to permit ease in computation.

The response function associated with line averaging of the horizontal velocity is dependent upon the instrument geometry and direction of the horizontal wind speed. For our sonic, which uses an orthogonal geometry in the horizontal plane, the following response function will be used to describe the effects of line averaging of the horizontal velocity:

$$T_{l_u}(n) = \frac{\sin^2(k_1 l_u/2)}{(k_1 l_u/2)^2} \quad [B7]$$

where l_u is the horizontal sonic path ($= l_w$ for our sonic). Figure B5 shows T_{l_w} and T_{l_u} as functions of $k_1 l$.
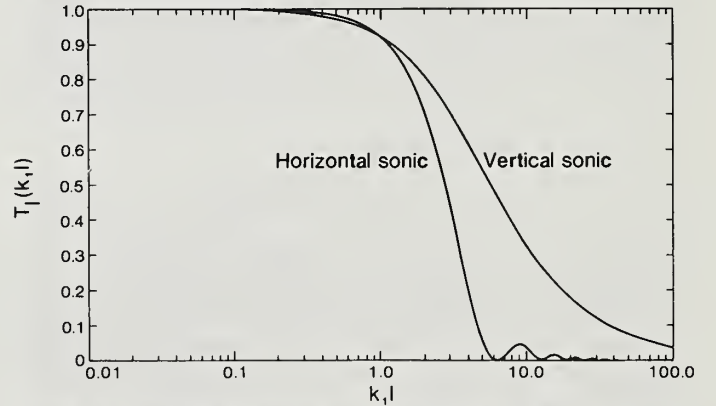
Figure B5.—Spectral transfer functions, $T_{1_w}(k_1 l_w)$ and $T_{1_u}(k_1 l_u)$, associated with line averaging of the vertical and horizontal wind velocity fluctuation measurements by the sonic anemometer.

These two response functions assume that line averaging takes place over a single acoustic path; however, our sonic (and many others as well) actually employs two parallel acoustic paths. Horst (1973b) found that the effect of path separation was not significant in the vertical direction, and after a similar investigation, we found that for our sonic the path separation effects were negligible in the horizontal as well.

Temperature Sensor

For the platinum wire resistance thermometer that we are using, response functions for both line averaging effects and the response of a first order system will be included.

The response time of this thermometer is given by Kaimal (1968) as follows: $\tau = 0.039/(1+\sqrt{3u})$, where u is measured in meters per second. Again we are assuming that this sensor is a first order sensor and we use equation [B2] for describing the dynamic frequency response. The response function appropriate to line averaging (of a scalar quantity like temperature as opposed to a vector quantity like the vertical velocity) was first developed by Gurvich (1962) and later extended by Silverman (1968). For ease of computation, their results have been adapted to give the following form:

$$T_l(n) = \frac{2\Gamma(4/3)}{\Gamma(1/2)\,\Gamma(5/6)\,(k_1 l)^2} \int_0^\infty \left[\frac{\sin^2(k_1 l x_3/2)}{(x_3/2)^2}\right]$$

$$\left[\frac{1}{(1+x_3^2)^{4/3}}\right]dx_3 \quad [B8]$$

where l is the length of the platinum wire ($= 18$ cm in our case). Figure B6 is a graph of T_l as a function of $k_1 l$.

Sensor Separation

For a variety of practical reasons, sensors will always be separated from one another. Yet this separation will also cause an error in any flux measurement for which two separate quantities are being correlated. We follow Moore's (1986) suggestion that the following response function be used for describing both lateral and longitudinal separation effects:

$$T_s(n) = \frac{2^{1/6}}{\Gamma(5/6)}(k_1 s)^{5/6}\, K_{5/6}(k_1 s) \quad [B9]$$

where s is the separation distance and $K_{5/6}$ is the modified Bessel function of the second kind. Figure B7 shows a plot of T_s as a function of $k_1 s$. As Moore (1986) cautions, however, [B9] is most applicable when the separation distances are not too great, and it may also lead to a slight overestimate of the flux loss.
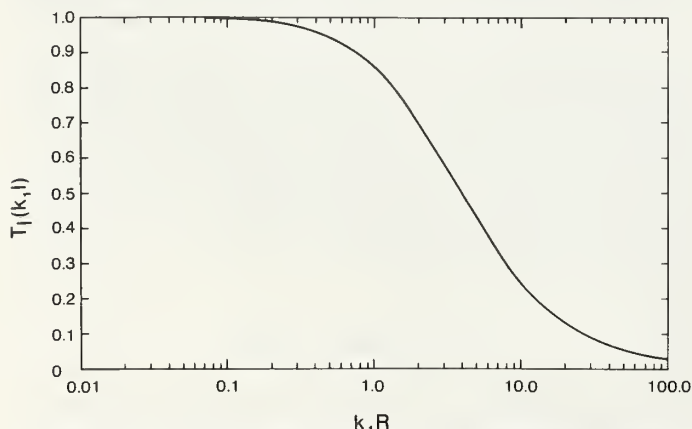

Figure B6.—Spectral transfer function, $T_l(k_1 l)$, associated with line averaging of the temperature fluctuation measurements by the platinum wire thermometer.
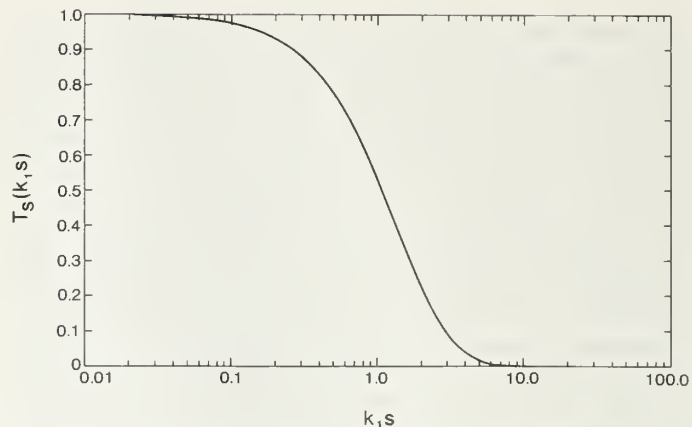

Figure B7.—Spectral transfer function, $T_s(k_1 s)$, associated with the spatial separation of any two eddy correlation instruments.

Data Logging System

Incorporated into our data logging system is a filter that also must be taken into account. This filter is a high pass recursive filter that is applied to all raw digitized sensor data to remove any linear or low frequency long-term trends from the data. These long-term trends can adversely affect the flux measurements (Kaimal 1975). The transfer function associated with this filter is approximated by Moore (1986) as follows:

$$T_R(n) = \frac{(2\pi n\tau_R)^2 a}{a+(2\pi n\tau_R)^2} \quad [B10]$$

where $a = e^{-1/(\tau' n_s)}$ and $\tau' = 200$ s (for our filter), and $\tau_R = a/[(1-a)n_s]$.

Aliasing

Aliasing results from sampling at uniform intervals any continuous signal that contains energy at frequencies above the Nyquist frequency. The Nyquist frequency, which is defined as one-half the sampling frequency, will henceforth be denoted by n_o. As a result of aliasing, spectral energy at frequencies above the Nyquist frequency can be folded back into the spectra at frequencies below the Nyquist frequency at harmonics of the sampling frequency. For example, the effects of aliasing upon measurements of $C_{wq}(n)$ can be written as follows (Kaimal et al. 1968):

$$C_{wq}^m(n) = \begin{cases} H_{wq}(n)C_{wq}(n)+\sum_{j=1}^\infty \left[H_{wq}(jn_s-n)C_{wq}(jn_s-n)\right. \\ \left.+H_{wq}(jn_s+n)C_{wq}(jn_s+n)\right] & 0\leq n\leq n_o \\ 0 & n>n_o \end{cases} \quad [B11]$$

where $C_{wq}^m(n)$ is the measured cospectra of w and q. Here the effects of the sensor response functions and the filters associated with the data logging system are included as components of $H_{wq}(n)$. The summation term of [B11] is the aliased portion of the measured cospectra. Although not specifically included in [B11], any spectra or cospectra can also be contaminated by aliased high

frequency noise associated with the electronics, nearby power lines, or any other outside power source. For sensors with short response times (such as sonic anemometers), antialiasing filters should be used to minimize the aliasing of any naturally occurring frequencies and to eliminate any high frequency contamination of the analog signal from outside sources. These antialiasing filters are usually designed as Butterworth or other similar filters. For sensors with relatively long response times (such as our vertical Gill propellers and chemical sensors), it is unnecessary to use an antialiasing filter because they will naturally accomplish these goals.

To include the effects of aliasing of the naturally occurring frequencies upon the flux loss computation, it is sufficient for our purposes to confine the consequences of aliasing to only the $(n-n_s)$ term of [B11]. Therefore, we can simply substitute the following expression for the integral given in the numerator of equation [B1]:

$$\int_o^{n_o} H_{wq}(n)C_{wq}(n)dn \; + \; \int_o^{n_o} H_{wq}(n_s-n)C_{wq}(n_s-n)dn$$

However, the above expression can be further simplified (by a change of variables) to the following:

$$\int_o^{n_s} H_{wq}(n)C_{wq}(n)dn$$

Therefore, equation [B1] can now be written in the following form:

$$\frac{\Delta F}{F} = 1 - \frac{\int_o^{n_s} H_{wq}(n)C_{wq}(n)dn}{\int_o^\infty C_{wq}(n)dn} \qquad [B12]$$

It is this last equation that was used to estimate the percentage flux loss from measurements taken with our system. The sampling frequency, n_s, of our system is about 14 Hz; this value will be used for all computations presented herein.

To include the influence of the antialiasing filter is quite simple with [B12] because in essence these filters are designed specifically to confine the effects of aliasing to only the $(n-n_s)$ term of [B11]. Therefore, all that needs to be done is to include as part of $H_{wq}(n)$ the spectral response function of a particular antialiasing filter. For example, a 2-pole Butterworth filter has a response function given as:

$$T_B(n) = 1 \Big/ \left(1 + (\frac{n}{n_o})^4 \right)^{1/2} \qquad [B13]$$

Other types of antialiasing filters are also easily included in the computations for the flux loss. However, before proceeding to the flux loss computation, we need to define the atmospheric cospectra, $C_{wq}(n)$, that will be used in [B12].

Atmospheric Cospectra

For the purposes of this work, the cospectra of momentum and sensible heat are the same for stable atmospheric conditions and are given by:

$$C_{uw}(n) = C_{wT}(n) = \frac{1}{1 + 2.34(z/\bar{u})^{2.1}n^{2.1}} \qquad [B14]$$

where z is the height of the sensors array above the zero plane displacement of the surface (z = 6 m for our site). This expression is taken from Kaimal et al. (1972), and although the normalization is not necessarily standard, for our purposes nothing more is needed. For unstable atmospheric conditions, the cospectra of momentum and sensible heat are different and given as follows:

$$C_{uw}(n) = \begin{cases} \dfrac{20.78}{[1+31(z/\bar{u})n]^{1.575}} & (z/\bar{u})n < 0.24 \\[2ex] \dfrac{12.66}{[1+9.6(z/\bar{u})n]^{2.4}} & (z/\bar{u})n \geq 0.24 \end{cases} \qquad [B15]$$

$$C_{wT}(n) = \begin{cases} \dfrac{12.92}{[1+26.7(z/\bar{u})n]^{1.375}} & (z/\bar{u})n < 0.54 \\[2ex] \dfrac{4.378}{[1+3.8(z/\bar{u})n]^{2.4}} & (z/\bar{u})n \geq 0.54 \end{cases} \qquad [B16]$$

These latter two equations were taken from Moore (1986).

For correcting the dry deposition fluxes of O_3, NO_2, and NO_x, we will assume that as atmospheric scalars, their cospectra are the same as that of temperature. There is some experimental evidence for the similarity between the spectra and cospectra of temperature and the spectra and cospectra of other scalars such as humidity and CO_2 (Redford et al. 1980, Smith and Anderson 1984, Ohtaki 1985, Anderson et al. 1986). However, no direct measurements of the spectra or cospectra of O_3, NO_2, or NO_x are available.

Atmospheric Spectra

With two simple modifications to [B12], the variance losses due to sensor limitations can be estimated in a manner completely analogous to that used for estimating the flux losses. First $H_{wq}(n)$ is replaced by the appropriate transfer function for a given instrument (i.e., H_w or H_c or H_T replaces H_{wq}) and, second, $C_{wq}(n)$ is replaced by the spectra appropriate to the quantity being measured.

For stable atmospheric conditions, the following variance spectra, taken from Moore (1986), will be used:

$$S_{qq}(n) = \frac{1}{1 + a_q[(z/\bar{u})n]^{5/3}} \qquad [B17]$$

where q refers to vertical velocity or temperature or any trace gas (O_3, NO_2, or NO_x). Again, the spectra associated with the trace gases is assumed to be the same as that associated with temperature. For q = vertical velocity, $a_q = 3.124[0.838 + 1.172(z/L)]^{-5/3}$, and for q = temperature, $a_q = 3.124[0.0961 + 0.644(z/L)^{3/5}]^{-5/3}$. Here z/L is the measure of atmospheric stability and is defined as $-kgz\overline{w'\theta'}/(u_*^3\bar{T})$ where L refers to the Monin-Obukhov length, k is the von Karman constant (= 0.41), g is the acceleration due to gravity (= 9.8 m/sec²), $\overline{w'\theta'} \approx 1.05 \overline{w'T'}$ at our site with θ being the potential temperature, and u_* is the friction velocity ($u_* \equiv (-\overline{u'w'})^{1/2}$). For stable conditions z/L is positive, and for unstable conditions z/L is negative. Neutral stability refers to z/L = 0.

For an unstable or neutral atmosphere ($z/L \le 0$), the vertical velocity variance spectra is taken from Højstrup (1981) and the temperature variance spectra is taken from Kaimal et al. (1972).

$$S_{ww}(n) = \frac{1}{1 + 5.3[(z/u)n^{5/3}]} + \frac{16(-z/L)^{2/3}}{[1 + 17(z/u)n]^{5/3}} \quad [B18]$$

$$S_{TT}(n) = \begin{cases} \dfrac{14.94}{[1 + 24(z/u)n]^{5/3}} & (z/u)n < 0.15 \\[3mm] \dfrac{6.827}{[1 + 12.5(z/u)n]^{5/3}} & (z/u)n \ge 0.15 \end{cases} \quad [B19]$$

With all the above simplifying assumptions in mind, we applied these response functions and atmospheric cospectra to our eddy correlation system. For the vertical Gill propeller, $H_w(n) = T_d^w(n)T_R(n)$ where the w subscript and superscript refer to the vertical velocity sensor and $H_w(n)$ is the spectral response function for this instrument. Likewise, for the horizontal propellers, $H_u(n) = T_d^u(n)T_R(n)$; for the temperature sensor $H_T(n) = T_d^T(n) T_l^T(n)T_B(n)T_R(n)$, and finally for the chemical sensors $H_c(n) = T_d^c(n)T_R(n)T_v(n)$. For the vertical sonic $H_w(n) = T_{l_w}(n)T_B(n)T_R(n)$ and for the horizontal sonic $H_u(n) = T_{l_u}(n)T_B(n)T_R(n)$. Therefore, the total system response functions for heat and momentum and chemical fluxes are given, respectively, as follows:

$$\left. \begin{aligned} H_{wT}(n) &= \sqrt{H_w(n)H_T(n)} \ T_s^{wT}(n) \ T_m^{wT}(n) \\[2mm] H_{uw}(n) &= \sqrt{H_u(n)H_w(n)} \ T_s^{uw}(n) \ T_m^{uw}(n) \\[2mm] H_{wc}(n) &= \sqrt{H_w(n)H_c(n)} \ T_s^{wc}(n) \ T_m^{wc}(n) \end{aligned} \right\} \quad [B20]$$

where the instrument separation and mismatching effects are denoted by $T_s(n)$ and $T_m(n)$, respectively, and the superscripts refer to that particular pair of instruments. It is important to note here that [B20] is an approximation. With [B20] we have "constructed" a response function. However, it is more appropriate to derive a response function for correcting the flux measurements similar to the way [B3], for example, was derived for correcting variance measurements; but, this more fundamental approach, except for the preliminary efforts of Kristensen and Fitzjarrald (1984), remains largely undeveloped both theoretically and observationally.

Computational Methods

Several different numerical methods were employed to evaluate equation [B12]. The denominator of this expression was evaluated analytically for the cospectra given by [B14], [B15], and [B16]. The numerator was evaluated numerically using the Romberg method of integration (Dahlquist and Bjorck 1974). The different transfer functions used for $H_{wq}(n)$ in [B20] were represented either directly by a specific analytical expression (e.g., [B2], [B5], [B10], and [B13]) or indirectly by a numerical table (e.g., [B3], [B6], [B7], [B8], and [B9]). The numerical

tables were provided by a simple evaluation of a function (e.g., [B7] and [B9]), or by the numerical evaluation of an integral (e.g., [B3], [B6], and [B8]). As with [B20], these latter three integrals were also evaluated with the Romberg method of integration. Finally, the numerical evaluation of [B20] sometimes required interpolating between points of the numerical tables representing [B3] and [B6] through [B8]. This was done using a quartic polynomial interpolator.

APPENDIX C.
Transfer Function for Volume Averaging

By using an intake tube to draw atmospheric samples into a reaction chamber, our chemical sensors average the turbulent fluctuations of O_3, NO_2, and NO_x over a spherical volume. Therefore, the spectral response of these sensors must degrade at higher wave numbers. This appendix provides a derivation of the response function associated with the volume averaging effects of the intake tube ($T_v(n)$ in equation [B3]), which can be used if necessary to correct the flux measurements for these effects. We begin by considering only spatial averaging effects; therefore, we will ignore other limitations of the sensors (such as a relatively long response time), which also influence the spectral response of these instruments.

From Andreas (1981) it is straightforward to show that the following relation holds between the measured constituent (O_3, NO_2, or NO_x) spectra, $\phi^m(\vec{k})$, and the true spectra, $\phi(\vec{k})$:

$$\phi^m(\vec{k}) = \frac{1}{\left(\frac{4}{3}\pi R^3\right)^2} \left[\int_{vol} e^{i\vec{k}\cdot\vec{s}}d\vec{s} \right] \left[\int_{vol} e^{-i\vec{k}\cdot\vec{s}'}d\vec{s}' \right]^* \phi(\vec{k}) \quad [C1]$$

where $\vec{k}$ is the three-dimensional wave number and R is the radius of the volume over which we are averaging. In arriving at [C1] Andreas' (1981) results for a right circular cylinder have been modified to an expression appropriate to a sphere. We have chosen the same right-handed coordinate system as he did (x = direction of the mean horizontal wind; y = direction in the horizontal plane perpendicular to the x axis; z = vertical direction = alignment direction of the intake tube). However, as in his case, the choice of this particular coordinate system is immaterial.

From [C1] it is clear the integral, $I = \int_{vol} e^{i\vec{k}\cdot\vec{s}}d\vec{s}$, must be evaluated. In cylindrical coordinates the integral is given by the following expression:

$$I = \int_0^{2\pi} \int_0^R \int_{-(R^2-z^2)^{1/2}}^{+(R^2-z^2)^{1/2}} e^{ik_3 z}e^{ir(k_1\cos\theta + k_2\sin\theta)} \, d\theta r dr dz \quad [C2]$$

where k_1, k_2, and k_3 are the three components of $\vec{k}$ along the x, y, and z axes. The integral over θ can be done explicitly (Andreas 1981) as can the integral over z (Silverman 1968, Wyngaard 1971), which yields:

$$I = 2\pi \int_0^R \frac{\sin((R^2-r^2)^{1/2} k_3)}{k_3/2} J_0(r(k_1^2 + k_2^2)^{1/2}) r dr \quad [C3]$$

where J_0 is a Bessel function.

Then changing variables from r to $\frac{r}{R} = \sin\theta$ yields:

$$I = \frac{2\pi R^3}{(k_3 R)} \int_0^{\pi/2} \sin 2\theta \, \sin(k_3 R\cos\theta) \, J_0(R\sin\theta(k_1^2 + k_2^2)^{1/2})d\theta \tag{C4}$$

Finally, using [C1] and [C4], we have

$$T'(\vec{k},R) = \frac{9}{4(k_3 R)^2} \left[\int_0^{\pi/2} \frac{\sin 2\theta \, \sin(k_3 R\cos\theta)}{J_0(R\sin\theta(k_1^2 + k_2^2)^{1/2})} \, d\theta \right]^2 \tag{C5}$$

where $T'(\vec{k},R)$ is defined as $\phi^m(\vec{k})/\phi(\vec{k})$.

However, only the one-dimensional spectra is observable and the true and measured one-dimensional spectra (denoted by $\Psi(k_1)$ and $\Psi^m(k_1)$, respectively) are related to $\phi(k)$ as follows:

$$\Psi(k_1) = \iint_{-\infty}^{\infty} \phi(\vec{k})dk_2 \, dk_3 \tag{C6}$$

$$\Psi^m(k_1) = \iint_{-\infty}^{\infty} \phi^m(\vec{k})dk_2 \, dk_3 = \iint_{-\infty}^{\infty} T'(\vec{k},R)\phi(\vec{k})dk_2 dk_3 \tag{C7}$$

The transfer function we seek, $T_v(n)$, is defined as $\Psi^m(k_1)/\Psi(k_1)$. With this in mind, the integrals for $T_v(n)$ (viz., C5, C6, and C7) can be computed once $\phi(\vec{k})$ is specified. Assuming local isotropic turbulence, the atmospheric variance spectra for a scalar quantity is given simply as $\phi(\vec{k}) = Ak^{-11/3}$ where A is a constant and k is the magnitude of $\vec{k}$. Therefore, $T_v(n)$ can be defined as follows:

$$T_v(n) = \frac{\iint_{-\infty}^{\infty} k^{-11/3}T'(\vec{k},R)dk_2 \, dk_3}{\iint_{-\infty}^{\infty} k^{-11/3}dk_2 \, dk_3} \tag{C8}$$

The denominator can be evaluated analytically to give $6\pi/5 \, k_1^{-5/3}$. With this last result [C8] and [C5] are equivalent to equations [B3] and [B4] of appendix B and all that remains is to note that $x_2 = k_2/k_1$ and $x_3 = k_3/k_1$ and to change variables of integration appropriately.

The integrals given in [B3] and [B4] were evaluated numerically using the Romberg method of integration (Dahlquist and Bjorck 1974). The Bessel function J_0 was also evaluated numerically using rational functions and rational polynomial approximations of J_0 (Press et al. 1986). Finally, because evaluating $T_v(n)$ required evaluating a triple integral, some care in design and testing of the computer code was necessary in order to assure that figure B4 is a good representation of $T_v(n)$.

APPENDIX D. Table of Symbols

Symbol	Definition	Unit
c	pollutant concentration	kg/m³ or ppb/v
$C_{wq}(n)$	atmospheric cospectrum of w and q as a function of n	
D	Gill propeller anemometer response length	m
F	corrected pollutant flux	kg/m²/s or (ppb/v)(m/s)
F_m	measured pollutant flux	kg/m²/s or (ppb/v)(m/s)
g	acceleration due to gravity	m/s²
$H_{wq}(n)$	total cospectral response function for vertical wind w and quantity q as a function of frequency	
k	von Karman constant	
k_i	spectral wave number in ith direction	cycles/m
L	Monin-Obukov length	m
n	frequency	s⁻¹
q	specific density of an arbitrary measured quantity	
Q	flow rate	liters/min
r_s	surface resistance	s/m
r_t	total transfer resistance	s/m
r_{wc}	correlation coefficient between w and c	

29

R	radius	m
$S_{qq}(n)$	variance spectra for any quantity q as a function of n	
t	time	s
T	temperature	°C
$T_B(n)$	response function for Butterworth filter	
$T_d(n)$	response function for dynamic frequency response	
$T_l(n)$	response function for line averaging	
$T_m(n)$	response function for mismatched sensors	
$T_R(n)$	response function for high-pass recursive filter	
$T_s(n)$	response function for sensor separation	
$T_v(n)$	response function for volume averaging	
u	horizontal wind speed	m/s
u_*	friction velocity	m/s
v_d	deposition velocity	cm/s
w	vertical wind speed	m/s
x_i	k_i/k_1, $i = 2,3$	
z	vertical coordinate	
z/L	stability parameter: measurement height divided by Monin-Obukov length	
z_0	roughness length	cm
σ_T^2	temperature variance	$(°K)^2$
σ_c^2	variance of c	$(ppb/v)^2$
σ_w^2	vertical velocity variance	$(m/s)^2$
θ	potential temperature	°K
ρ_c	density of pollutant c	g/m^3
τ	sensor response time	s
φ	phase angle due to sensor mismatch	
ψ_c	universal stability influence function	

   The Pawnee Grassland Eddy Correlation Dry Deposition Project is
described. Instrumentation, methods of analysis, and initial data and
research findings are presented. Data from this eddy correlation
system show agreement with (a) previous observations of deposition
velocities for atmospheric ozone, NO_2, and NO_x; (b) micrometeorolog-
ical theory; and (c) micrometeorological site characteristics.

Keywords: Eddy correlation, dry deposition, Pawnee Grasslands, O_3,
NO_2, NO_x, micrometeorology

U.S. Department of Agriculture
Forest Service
Rocky Mountain Forest and Range Experiment Station

Rocky Mountains

Southwest

Great Plains

The Rocky Mountain Station is one of eight regional experiment stations, plus the Forest Products Laboratory and the Washington Office Staff, that make up the Forest Service research organization.

RESEARCH FOCUS

Research programs at the Rocky Mountain Station are coordinated with area universities and with other institutions. Many studies are conducted on a cooperative basis to accelerate solutions to problems involving range, water, wildlife and fish habitat, human and community development, timber, recreation, protection, and multiresource evaluation.

RESEARCH LOCATIONS

Research Work Units of the Rocky Mountain Station are operated in cooperation with universities in the following cities:

Albuquerque, New Mexico
Flagstaff, Arizona
Fort Collins, Colorado*
Laramie, Wyoming
Lincoln, Nebraska
Rapid City, South Dakota
Tempe, Arizona

*Station Headquarters: 240 W. Prospect St., Fort Collins, CO 80526